Understanding functional dynamics and conformational stability of beta-glycosidases

Ben Bdira, F.

CHAPTER 4

Exploring the Conformational Landscape and the Dynamics of GH11 xylanases During Catalysis

Abstract

GH11 xylanases are a family of β-glycosidases involved in the degradation of hemicellulose, one of the major components of renewable biomass. This family of enzymes has attracted increased attention due to their potential industrial applications, especially in biofuel production. To explore the conformational landscape and the dynamics of GH11 xylanases during catalysis, *Bacillus circulans* (BCX) xylanase was used as a model. By combining paramagnetic NMR spectroscopy with Carr-Purcell-Meiboom-Gill relaxation dispersion (CPMG RD) techniques, the millisecond dynamics and conformational changes of BCX in each step of its catalytic reaction were studied. To study the Michaelis-Menten complex a catalytically inactive variant of BCX was used in the presence of xylohexaose (X6); the glycosyl-enzyme intermediate was trapped using a novel epoxide compound, epoxy-Xylobiose (epoxyX2) that forms a stable adduct with the nucleophilic residue. The last step of the reaction, the product release, was studied in the presence of xylobiose (X2). In the free state, the protein adopts a ground state that resembles its crystal conformation showing millisecond dynamics in its "fingers" and "thumb" regions. Substrate binding to BCX follows an induced fit mechanism as revealed from the NMR titration data. The exchange rate between the open bound and the closed bound protein conformations is in the range of its substrate turnover rate, suggesting a role for such movement in the enzymatic reaction. Both of the enzyme bound states conformations are different from the one of the free state, as revealed by PCS data. Structural differences are located within the β-strands and the thumb that sculpture the enzyme binding cleft. X6 binding induces a global enhancement of the protein millisecond dynamics for the same regions that experience conformational changes. Such millisecond dynamics enhancement might reflect the role played by the protein motion in substrate positioning and sugar rings distortion.

In the covalent glycosyl-enzyme complex dynamics in the millisecond timescale is similar to that of the free enzyme. Nevertheless, covalent complex formation causes significant conformational changes located in the thumb and in the vicinity of the catalytic residues, as revealed by chemical shift perturbations and PCSs. In the product enzyme complex, the protein experiences subtle conformational changes compared to its free state, yet significant changes of its dynamic behaviour are observed. It is hypothesised that the protein motion in its product complex is playing a role in product dissociation from the catalytic site.

The protein ground states in the Michaelis-Menten and in the product complexes sample excited states that share a similar conformation with the glycosyl-enzyme complex ground state, which is suggested by the correlations between the chemical shift changes derived from the CPMG RD data fits and the chemical shifts of the intermediate state.

In summary, BCX samples at least five ground states during catalysis and the rate limiting step of the reaction is possibly due to the high energy barrier that separates the adopted conformations in the Michaelis-Menten complex. The protein grounds states are connected by an excited state that resembles the intermediate state conformation.

To be submitted for publication

Introduction

Chemical reactions in living organisms occur at an ominously higher rate than their spontaneous counterparts as a result of a decrease of the transition state energy of the reaction by highly sophisticated catalysts called enzymes. In the past decades, understanding enzyme function has been revolutionized by determining snapshots of their 3D structures at an atomic resolution using X-ray crystallography, paving the way for describing their structure/function relationships. Despite this great triumph, the obtained static structures cannot always explain the elusive catalytic function of enzymes. Later on, it became evident that proteins in general, including enzymes, are dynamic entities that sample a large ensemble of conformations around an average structure. The time scale of these structural fluctuations in combination to their amplitudes and directions have proven to be the missing piece of the puzzle necessary to achieve a better understanding of enzyme function. The conformational space that can be explored by a protein is referred to its "energy landscape" in which its native conformation populates a low-energy state called "ground states", which is in a continuous exchange with higher energy conformations called "excited states"[1, 2]. The exchange kinetics between the protein conformers is dictated by the amplitude of the energy barrier that separates the different states. Excited states that are separated by a high energy barrier, interconvert on the microsecond to millisecond time scale or longer. Those "excited states" have been associated with enzyme molecular function, including ligand binding[3, 4] and catalysis [5, 6].

NMR spectroscopy and X-ray crystallography are the techniques of choice to determine the protein ground state structures. However, each technique has its limitations and challenges, for instance structure calculation by NMR spectroscopy remains a laborious method limited by the protein size and the quality of its NMR spectra. X-ray crystallography does not always capture the in-solution conformation of the ground state, due to crystal packing artefacts. Moreover, in the presence of their ligands, enzymes can experience conformational changes in solution that may not be visible in the crystalline state. Recently, paramagnetic NMR spectroscopy has emerged as an approach that bridges both techniques by providing structural restraints in solution that can be used to validate protein conformations in the crystalline state[7]. For instance, pseudocontact shifts (PCSs) provide long range restraints. They are caused by magnetic susceptibility anisotropy of a paramagnetic metal ion, described by a tensor, the $\Delta\chi$-tensor[7]. PCSs have been used in crystal structure refinement[8] and also exploited to determine the structure of a short-lived enzyme intermediate state[9]. These advanced applications of PCSs in the field of structural biology benefit from rigid lanthanide tags such as CLaNP-5[10]. On the other hand, the characterisation of the excited state conformers and the understanding of their interconversion mechanisms with the enzyme ground-state remains a challenge, due

to their short lifetime and their lowly populated fraction compared to the ground state. By virtue of the recent development of NMR spectroscopy techniques it is possible now to probe those "invisible" states and characterize their thermodynamics and kinetics properties. One of the most successful techniques is the Carr-Purcell-Meiboom-Gill relaxation dispersion (CPMG RD)[11, 12]. It has been applied to dissect the energy landscape of enzymes during catalysis in combination with lower resolution techniques[13-15]. However, the most successful RD studies profited from the availability of enzyme conformations of consecutive steps of catalysis captured in the crystalline state, a situation that is not accessible for most enzymes[13, 15].

One of the prominent enzyme classes in nature are glycosyl hydrolases (GHs), which are classified in more than 140 families in Cazy the database[16]. GH11 xylanases are GHs able to hydrolyse the endo β-1-4-glycosidic link of xlyan polymers, the main components of hemicellulose and the second most abundant renewable biomass material[17]. This family of enzymes attracted an increasing attention in the last decades due to their potential applications in industry and, especially, in biofuel production[18]. Therefore, the quest to find the optimum conditions for their large-scale industrial applications has boosted research to understand their structure/function relationship. GH11 xylanases have a characteristic fold, a β-jelly roll fold with a highly conserved amino acid sequence for the residues lining the binding site. The superposition of more than forty available crystal structures from different organisms revealed a remarkable conservation of the β-jelly roll domain topology as indicated by the small Cα atom RMSD (<1.5 Å)[19]. The overall shape of the GH11 fold is often compared to a right-hand fist. It includes β-strands A which are nearly planar and distorted at the end to form a "hand palm" and "fingers", and β-strands B perpendicular to β-strands A, sculpting the binding cleft and including the "thumb" region. The two sides of the cleft are connected by a long loop called the "cord". The fold includes a single α-helix, sitting under the β-strands B structure (**Figure 4.1a**). The topographical properties of the catalytic cleft of GH11 xylanases are highly conserved with an approximate depth of 9 Å, a width of 4 Å and length of 25 Å. The position of the catalytic dyad in the middle of catalytic cleft is in agreement with their endo catalytic mechanism. The thumb region displays a well-structured classical hairpin, containing a type I β-turn with six internal hydrogen bonds. Among GH11 members the primary structure of this loop is conserved, suggesting a key role for function[20]. One of the best characterized GH11 xylanases member is the endo β-1-4 xylanase from *Bacillus circulans* (BCX). This enzyme has been extensively studied by X-ray crystallography[21] and NMR spectroscopy[22] due to its low molecular weight (20 kDa, like other GH11 members) and its apparently rigid and globular structure. The binding cleft of BCX has at least three (-) subsites (glycon binding site) and three (+) subsites (aglycon binding sites) according to the nomenclature of Davies et al.[23]. The glycosidic bond hydrolysis of xylan

polymer takes place between the -1/+1 subsites with a substrate binding in at least the -2/-1 and +1 subsites in accordance with the protein endo catalytic mechanism.

BCX, like other GH11 members, employs the "Koshland" double displacement mechanism with a catalytic nucleophile and acid/base for catalysis[24]. After substrate binding within the enzyme binding cleft (**ES** complex), a nucleophilic attack by the catalytic amino acid to the anomeric carbon of the glycosidic substrate occurs. Concomitantly, a proton transfer from the acid/base residue followed by departure of the leaving group from the aglycon site takes place during the first catalytic phase, from which an enzyme-glycoside covalent intermediate results (**EI** complex). In the next phase, an activated water molecule acts as a nucleophile with the assistance of the general acid/base to deglycosylate the catalytic residue through an oxocarbenium ion transition state. The final step is the product release from the enzymatic pocket (**EP** complex) (**Figure 4.1b**). The chemistry behind this hydrolysis function is widely accepted. Although several studies, mainly based on molecular dynamics calculations[25-27] have provided some insights, a complete understanding of the conformational changes and dynamics of BCX during catalysis is still lacking. For instance, molecular dynamics simulations have suggested the opening of the thumb loop to induce the product dissociation[25-28]. The only evidence of a full opening of the thumb was observed in the case of a xylanase mutant from *B. subtilis* in the crystalline state[29]. A recently published study of GH11 xylanase millisecond time scale dynamics using the CPMG RD technique showed that the protein in its free form experiences a millisecond motion for multiple residues localized within the binding site[30]. In the presence of its substrate (**ES**), an enhancement of the millisecond (ms) time scale motion was observed[30]. This study has provided the first evidence of such dynamics behaviour in GH11 family enzymes. A thorough MD investigation on GH11 family enzymes was undertaken in XYNII from *Trichoderma reesei.* [31]. By combining the different crystal structures of the enzyme, it was proposed that the protein samples three sequential substates during its catalytic reaction. First, the protein adopts an open state to accommodate the substrate in the cleft. Substrate binding induces a closed conformation necessary for positioning the substrate into the correct configuration for glycosidic bond hydrolysis. The last state is a loose structure from which the product is released. The study provided a first model for the enzyme catalytic cycle based on the available crystal structures, which still needs to be validated with in solution studies.

In the present work, paramagnetic NMR and CPMG RD techniques were combined to characterize GH11 xylanases in each step of their catalytic cycle using BCX as a model. First, the in-solution average conformations of the enzyme in its $\mathbf{E}_{\text{free}}$ as well as **ES**, **EI** and **EP** forms were studied by PCSs. To characterize the **ES** complex, a silenced version of the enzyme was generated by substituting the E78 nucleophile with a glutamine in the presence of xylohexose (X6). The **EI** complex was trapped by a novel compound epoxy-xylobiose (epoxyX2) that mimics closely the intermediate state of the reaction and forms a covalent adduct complex with the enzyme. The **EP** ground state conformation was

studied in the presence of xylobiose (X2) that appears to bind only to the -1/-2 subsites, thus emulating the last step of the reaction. The dynamic behaviour of each complex, separately, was also studied using CPMG RD, aiming to uncover the link between the ground and excited states. The implications for BCX catalytic function are discussed.

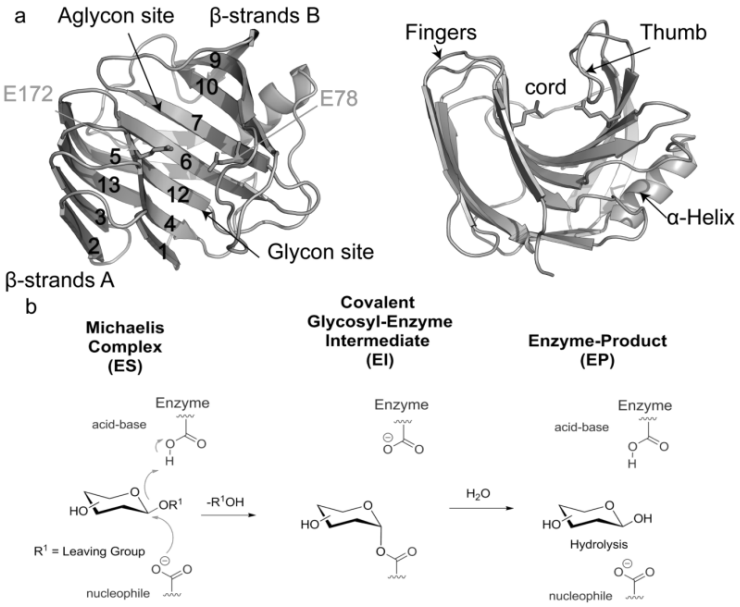

Figure 4.1. GH11 fold and catalytic mechanism. (**a**) β-jelly roll fold of *Bacillus circulans* xylanase with β-strands numbering. Glycon and aglycon binding sites of BCX binding cleft are indicated in arrows. The catalytic dyad in the middle of the binding cleft are shown in sticks. (**b**) General retaining β-glycosidases mechanism.

Results

BCX free state (E_{free}) in solution conformation

To investigate BCX conformational state in solution with an atomic resolution, pseudocontatct shifts (PCSs) were used. BCX PCSs were obtained by preparing diamagnetic and paramagnetic NMR samples through the attachment of Lu-CLaNP-5 and Yb-CLaNP-5 to ^{15}N labelled BCX T109C/T111C double mutant, respectively. The choice of the double mutations positions was based on the rigidity of the region and its exposure to the surface, as suggested by the protein crystal structure[32]. Positions for which the distance between the Cα atoms was between 8 to 10 Å, in accordance with the standard for CLaNP5[12] were selected, to warrant correct attachment of the lanthanide tag to the protein. A few double cysteines mutants at different positions were generated and tested for expression yield and stability and the optimal one was identified to be T109C/T111C (**Figure 4.2**).

The backbone nuclei of the diamagnetic and paramagnetic spectra were assigned using the wild type assignment[24]. By calculating the chemical shift differences between the paramagnetic and diamagnetic spectra 127 PCSs were obtained (**Figure 4.3a**). The experimental PCSs were used to determine the position of the lanthanoid ion and the size and the orientation of the $\Delta\chi$ tensor. The data was fitted to BCX crystal structure (PDB ID: 2bvv or 1bcx)[32] and the lanthanoid position was ~ 8 Å from the Cα atoms of both cysteines, which is in agreement the previously reported distances[10]. The magnitudes of the axial and rhombic parts of the tensor were determined to be $8.3 \pm 0.1 \times 10^{-32}$ m^3 and $2.1 \pm 0.1 \times 10^{-32}$ m^3, respectively. A correlation between the experimental and the predicted PCSs from BCX crystal structure was observed with a low Q factor value equal to 0.021 including all data (**Figure 4.3b**). Exceptions are residues G139, W58 and T44 which show slight deviations from predicted values. Overall, the PCSs are consistent with prior studies that revealed BCX is indeed globular and compact, mainly due the extensive hydrogen bonds network between its backbone amide groups[21, 22]. The compact conformation of BCX is also supported by study of the pico-nanosecond dynamics[33]. The protein exhibits restricted motion on the probed time scale. Nevertheless, these observations do not exclude the possibility of a slower protein motion, on the millisecond time scale.

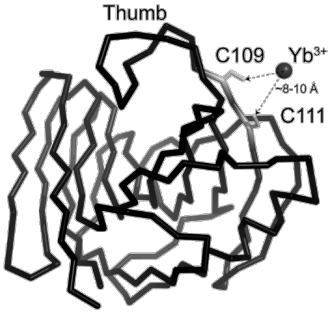

Figure 4.2. Locations of engineered Cys residue for CLaNP-5 attachment and the lanthanoid position on the BCX surface, depicted on the crystal structure (PDB ID:2bvv). BCX is shown in black Cα trace, cysteines in grey sticks and the lanthanoid in black sphere. The distances between the cysteines side chains and the lanthanoid are indicated.

E_{free} dynamics

To follow the millisecond time scale dynamics of BCX a relaxation dispersion TROSY-CPMG experiment at 293 K was performed. Forty-three residues show relaxation dispersion profiles ($R_{ex} > 1$ s^{-1}) clustered within the fingers, thumb and palm regions and in loops connecting β-strands 6 and 7 and the ones connecting β-strand 12 to the α-helix (**Figure 4.3c, d**). A global two-site exchange fit of 27 residues with $R_{ex} \geq 1.8$ s^{-1} yields an exchange rate (k_{ex}) between the ground and excited states of 2.5 ($\pm$0.09) $\times 10^3$ s^{-1} with an excited fraction (p_B) equal to 0.78 %, suggesting a lowly populated excited state with local ms time scale dynamics (**Figure 4.4a**).

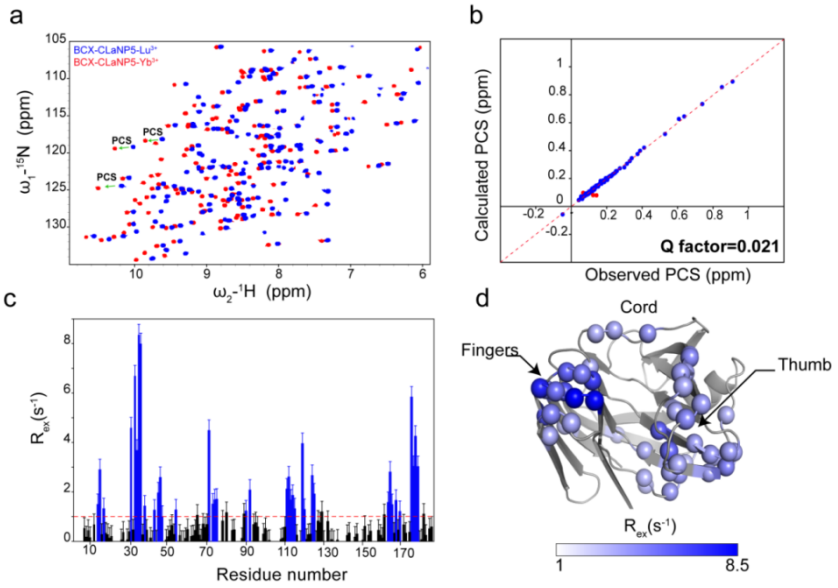

Figure 4.3. BCX free state conformation and dynamics in solution. (**a**) Overlay between BCX free state diamagnetic (BCX T09C/T111C-CLaNP-5-Lu^{3+}, blue) and paramagnetic (BCX T09C/T111C-CLaNP-5-Yb^{3+}, red) spectra. Three PCSs are highlighted with green arrows. (**b**) Plot of the observed vs. calculated PCSs after fitting to the BCX crystal structure (PDB ID:2bvv)[32]. Blue circles indicate PCSs of with high correlation factor (PCS deviation < 0.02) and red circles indicate PCSs of outliers (PCS deviation > 0.02). The dashed line represents a perfect correlation. (**c**) Plot of R_{ex} vs. residue numbers of BCX free state. Residues with $R_{ex} \geq 1\ s^{-1}$ are shown in blue bars. The error bars represent the estimated error based on a duplicate measurement of different ν_{CPMG} frequencies. (**d**) Amides with $1\ s^{-1} \leq R_{ex} \leq 8.5\ s^{-1}$ shown in spheres on the BCX crystal structure (PDB ID: 2bvv) and coloured with a white/blue gradient. Residues with $R_{ex} \leq 1 s^{-1}$ are shown in grey cartoon.

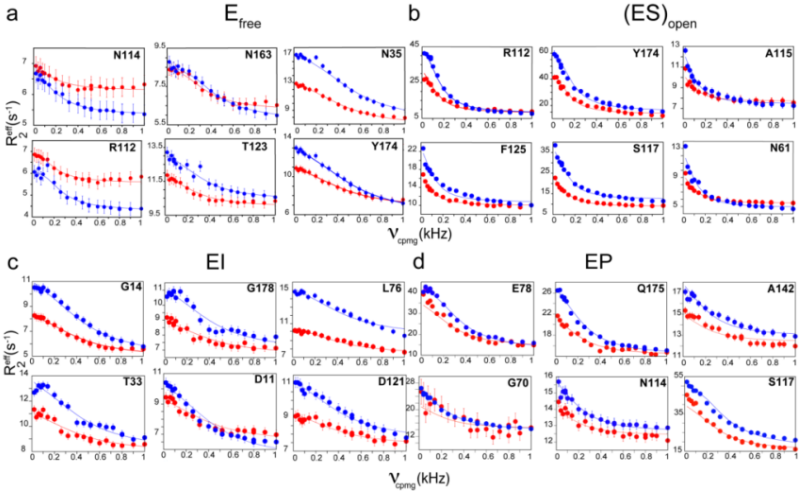

Figure 4.4: Global fit of CPMG RD data to a two-state chemical exchange model acquired on two static fields (red at 600 MHz and blue at 850 MHz) for (**a**) $\mathbf{E}_{free}$; (**b**) $(\mathbf{ES})_{open}$; (**c**) **EI**; (**d**) **EP**. Six residues with the best global fit profiles are shown for each state. Residue names are indicated.

BCX substrate complex (ES)

Michaelis-Menten binding

The first step of any enzymatic reaction is the formation of the Michaelis-Menten complex between the enzyme and its cognate substrate. GH11 xylanases binding sites are formed by multiple subsites that accommodate at least six sugar units of xylan polymer. The subsites are named -1/-2/-3 and +1/+2/+3 for the glycon and the aglycon binding cavities, respectively. BCX is able to hydrolyse the glycosidic link (between -1/+1 subsites) of at least three xylose units, where two of them have to be accommodated within the -1/-2 subsites and the remaining one in the +1 subsite.

To avoid substrate hydrolysis while investigating the Michaelis-Menten complex of BCX, the nucleophile residue E78 was substituted by a Q. ^{1}H-^{15}N heteronuclear single quantum correlation spectroscopy (HSQC) was used to monitor the titration of the inactive enzyme with xylohexaose (X6). The single amino acid substitution did not induce major changes of the protein HSQC spectrum, so the mutant assignment was performed using the wild peak list and curated by PCSs. Twelve titration points were acquired by increasing X6 concentration from 0 to 20 mM. Throughout the titration, significant line broadening (**Figure 4.5a**) in conjunction to diverse chemical exchange regimes of the side-chain and backbone amides were observed. Line broadening reflects an increase of the global tumbling time, which could be due to the changes of the buffer viscosity or due to weak self-association induced by X6. Similar observations were made when titrating the enzyme with X4[34].

Residues N54, A55, N141 and W185 exhibited a fast exchange behaviour ($k_{ex} >> \Delta\omega$) with progressive chemical changes and significant $\Delta\delta_{avg}$ (up to 0.4 ppm) (**Figure 4.6.a,c**). Those residues are located in the "knuckles" of the hand-like protein previously identified as a secondary binding site (SBS) of the substrate (**Figure 4.6d**)[34]. Peak shape analysis of the SBS residues revealed a K_d= 2.8 (±0.01) mM and a k_{off}= 5.7 (±0.12) × 10^3 s^{-1}. At 3.5 mM of X6 concentration, several secondary peaks start to appear in a slow exchange regime ($k_{ex} < \Delta\omega$) some of them appear in the vicinity of the amides primary peaks (**Figure 4.6b**). Among those secondary peaks, 32 were identified to be located within the enzyme binding cleft (primary binding site) and others scattered over the protein backbone. For instance, residues N8, G12 and K40 of the fingers and residues D119, G120, Y166 and V168 located within the thumb loop and its surrounding at the -1/ -2 /-3 subsites which exhibit clear splitting of their peaks. Moreover, residues of the +1/+2 subsites, such as Y65 and V81, experience the same phenomena. Variability in the linewidth of the secondary peaks was observed (**Figure 4.5b**). By performing a peak shape analysis of the titration data and fitting 16 backbone amides with a secondary peak to the "induced fit binding model", a correlation between the predicted versus the experimental peaks positions was obtained (**Figure 4.6b**). The k_d of the binding process

is equal to 1.9 (±0.015) mM and the k_{off}= 1.3 (±0.03) × 10^3 s^{-1}. The fit suggests that the ligand binds to the protein through an induced fit mechanism where the **ES** complex is in equilibrium between two conformations ($\mathbf{E}_{free}$+S→$(\mathbf{ES})_{open}$⇔$(\mathbf{ES})_{closed}$) with a k_{open} and k_{closed} equal to 11 and 9 s^{-1}, respectively. Additionally, residues distal from the enzyme binding cleft exhibit also chemical perturbations in the intermediate exchange regime (k_{ex}≈Δω) such as A152 and S155 of the α-helix with respective $\Delta\delta_{avg}$ = 0.3 and 0.18 ppm. The calculation of the average chemical shift perturbations ($\Delta\delta_{avg}$) between the backbone amides of the $(\mathbf{ES})_{open}$ and $\mathbf{E}_{free}$ confirmed the location of the amides with secondary peaks in the enzyme binding cleft (**Figure 4.6c,e**). The most important $\Delta\delta_{avg}$ are for residues located within the thumb and the finger regions. Residues of the α-helix such as A152 and S155 experience also large $\Delta\delta_{avg}$ in the $(\mathbf{ES})_{open}$ state despite their remote position from the primary and secondary binding sites which might suggests changes of the α-helix conformation upon ligand binding.

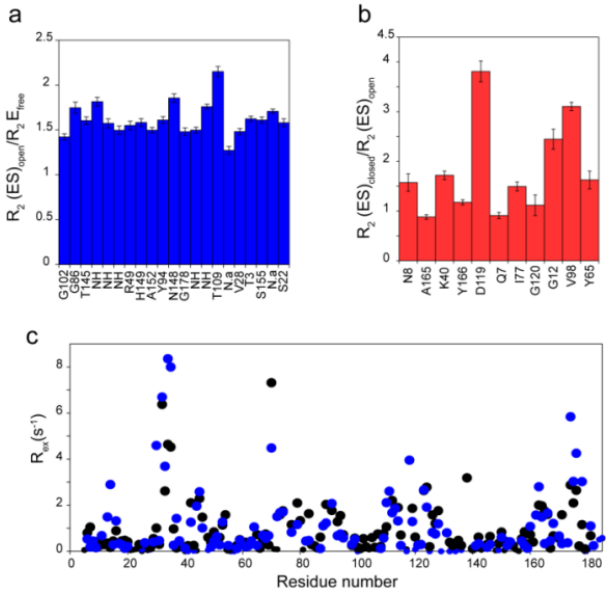

Figure 4.5: BCX E78Q NMR titration with X6 and its ms relaxation. (**a**) General line broadening of the BCX E78Q upon titration with X6. The ratios between R_2 values, predicted from the 2D peak shape analysis with TITAN, in the absence and the presence of 20 mM X6 from amides peaks that do not shift during titration. NH indicate side chain amides. N.a indicate non-assigned backbone amides. (**b**) the ratios between the $(\mathbf{ES})_{open}$ and $(\mathbf{ES})_{closed}$ R_2 values of the backbone amides in the slow exchange regime (k_{ex} << Δω). (**c**) Overlay between the R_{ex} values of the BCX WT (blue) and the BCX E78Q (black).

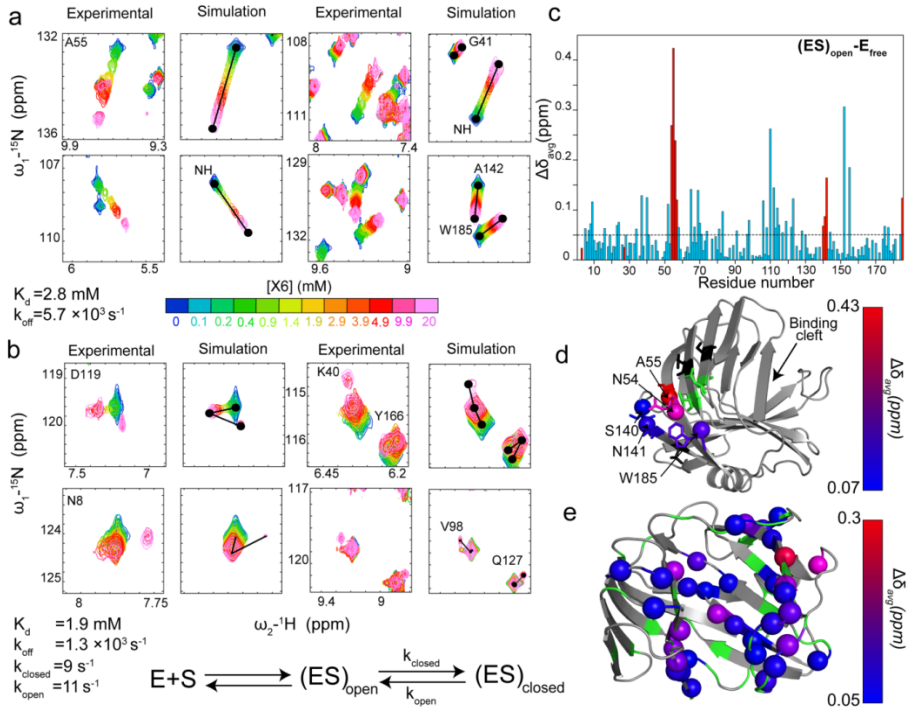

Figure 4.6. BCX E78Q titration with X6 (ES complex). (**a**) Experimental versus simulated chemical shift perturbations of backbone and side chain amides (NH) in the fast exchange regime ($k_{ex} >> \Delta\omega$) that belong to the secondary binding site. The simulation was performed using TITAN[35] software and the binding kinetics parameters are indicated. (**b**) Experimental chemical shift perturbations of BCX E78Q backbone amides with slow chemical regime ($k_{ex} < \Delta\omega$) versus their simulated chemical shift perturbations using an induced fit binding model. The kinetic parameters are indicated with a scheme of the enzyme-substrate interaction. (**c**) $\Delta\delta_{avg}$ between the (**ES**)$_{open}$ and the **E**$_{free}$ plotted versus residue numbers. $\Delta\delta_{avg}$ of the secondary binding site amides are shown in red bars. (**d**) Amide groups of the secondary binding sites with $\Delta\delta_{avg} > 0.05$ ppm mapped on the BCX crystal structure (PDB ID: 1bcx)[21] in spheres and sticks and coloured by the amplitude of the $\Delta\delta_{avg}$ using a blue/red colour gradient. Residues for which no data were obtained are coloured in green and the ones with $\Delta\delta_{avg} < 0.05$ ppm in black. (**e**) Amide groups of the binding cleft with $\Delta\delta_{avg} > 0.05$ ppm, including amides with a secondary peak, mapped on the BCX crystal structure (PDB ID: 1bcx) in spheres and coloured by the amplitude of the calculated $\Delta\delta_{avg}$ using a blue/red colour gradient. Residues for which no data was obtained are coloured in green and the ones with $\Delta\delta_{avg} < 0.05$ ppm in grey.

ES conformations

To interrogate the conformational changes of BCX in the **ES** complex an X6 titration of the protein was performed using diamagnetic and paramagnetic NMR samples (^{1}H-^{15}N BCX E78Q T109C/T111C tagged with CLaNP5). Similar chemical exchange regimes during titration were observed as for BCX E78Q. The chemical shift differences between the paramagnetic and diamagnetic NMR spectra of the protein in the presence of 20 mM X6 were calculated and 105 PCSs were obtained for the (**ES**)$_{open}$. Ten PCSs were also calculated for (**ES**)$_{closed}$. Fitting of the PCS data vs. the crystal structure of the free protein yielded small variations between the tensors obtained for the **E**$_{free}$ and (**ES**)$_{open}$ states

(**Figure 4.7**), suggesting that the lanthanoid moves slightly or the tensor reorients. As the structure of the $(\mathbf{ES})_{open}$ state is not available, it was decided that the PCSs were best compared using the structure of the free enzyme and the tensor obtained for that state. Thus, observed PCSs of the $(\mathbf{ES})_{open}$ were compared to the PCSs predicted from BCX crystal structure (PDB ID:2bvv) using the tensor parameters of the $\mathbf{E}_{free}$ state. Eighty-seven PCSs show a good fit with the protein crystal and multiple outliers were observed (Q=0.115), which suggests conformational differences between the $\mathbf{E}_{free}$ and $(\mathbf{ES})_{open}$ states (**Figure 4.8a**). When mapped on the protein structure, the amides outliers are seen to be located within the thumb, the α-helix and the finger regions (**Figure 4.8b**).

The PCSs differences (ΔPCSs) between the $(\mathbf{ES})_{open}$ and $\mathbf{E}_{free}$ were calculated and plotted vs. residue numbers (**Figure 4.9.c**). It reveals that at least five regions of the protein backbone experience significant changes of their conformation ($|\Delta PCS| > 0.02$ ppm) upon substrate binding and they are approximately clusters between W9-N20 and T33-N35 in the fingers; Y65-Y69 in the middle of hand palm close, to the nucleophile catalytic residue E78; A115-S117 in the thumb and A165-G173 in the hand palm, which accommodates the acid/base catalytic residue. When mapped on the protein crystal structure, those regions are spanned all over the protein β-jelly roll fold including the fingers, the thumb, the cord, the α-helix and the palm-hand (**Figure 4.9d**). This suggest that upon substrate association, the protein experiences a global conformational change. Additionally, by comparing the 10 experimental PCSs of the $(\mathbf{ES})_{open}$ and with their counterparts in the $(\mathbf{ES})_{closed}$, three of them show weak structural correlation between the two states (**Figure 4.8c**). Those residues include D119 located on the tip of the thump loop and I107 and V168 positioned deep in the binding cleft (**Figure 4.8d**). Thus, $(\mathbf{ES})_{open}$ and $(\mathbf{ES})_{closed}$ conformations might be also different at least within the thumb and hand palm regions.

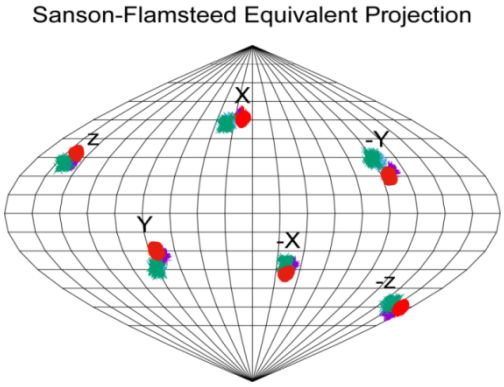

Figure 4.7: $\mathbf{E}_{free}$, $(\mathbf{ES})_{open}$, EI and EP tensors parameters and precision. One hundred $\Delta\chi$ tensors generated from jackknife analysis within Numbat for $\mathbf{E}_{free}$ (cyan), $(\mathbf{ES})_{open}$ (purple), **EI** (red) and **EP** (green) placed at the center of a sphere. The locations where the X, Y, and Z components pierce the sphere are indicated. The surface of the sphere is shown as a Sanson-Flamsteed equivalent projection with gridlines at every 20° (vertical) and 10° (horizontal).

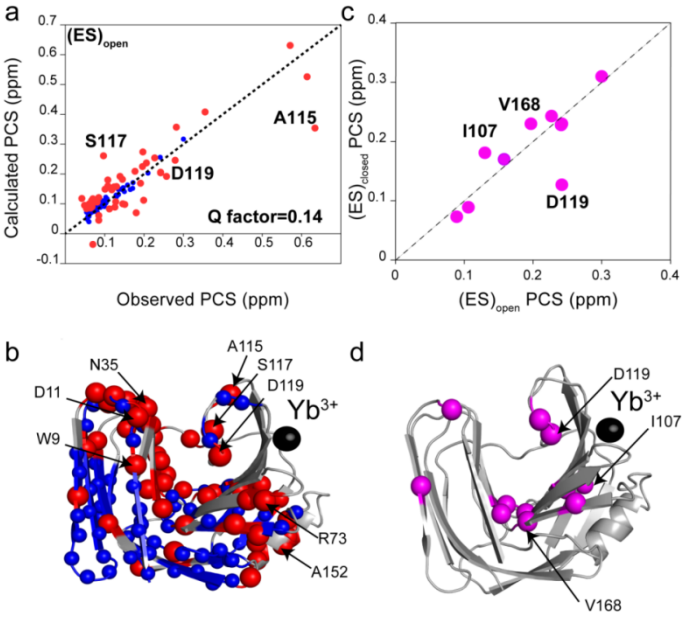

Figure 4.8. ES conformational states in solution probed by PCSs. (**a**) Plot of the $(\mathbf{ES})_{open}$ observed vs. calculated PCSs after fitting to the BCX crystal structure (PDB ID:2bvv). Blue circles indicate PCSs with high correlation (PCS deviation < 0.02) and red circles indicate PCSs of outliers (PCS deviation > 0.02). The dashed line represents a perfect correlation. (**b**) $(\mathbf{ES})_{open}$ observed PCSs mapped on the BCX crystal structure (PDB ID:2bvv) shown in spheres. Blue spheres indicate amide residues with high correlation to the back calculated PCSs and red spheres represent outliers. Residues with no observed PCSs are shown in grey cartoon. (**c**) Plot of observed PCSs of the $(\mathbf{ES})_{open}$ vs. the $(\mathbf{ES})_{closed}$ states. The dashed line represents a perfect correlation. (**d**) Amides for which the $(\mathbf{ES})_{closed}$ PCS could be measured mapped on the BCX crystal structure (PDB ID:2bvv). The black spheres indicate the position of the lanthanide (Yb^{3+}).

ES millisecond dynamics

To investigate the dynamics of BCX in the **ES** complex, its ms time scale motions were probed. Previous study has shown a local change of a BCX protein homologue backbone dynamics when substituting the nucleophile with Ala[30]. In the present study, the substitution E78 by Q did not cause significant changes of the protein dynamics behaviour (**Figure 4.5c**). Thereafter, a TROSY-CPMG experiment of BCX E78Q in the presence of 20 mM X6 (> 90% saturation of the primary binding site) was acquired. By analysing the relaxation dispersion profiles of the backbone amides of the $(\mathbf{ES})_{open}$, a remarkable enhancement of the chemical exchange was observed, as can be concluded from a comparison of R_{ex} values between the $(\mathbf{ES})_{open}$ and $\mathbf{E}_{free}$ states (**Figure 4.9a**). Multiple protein regions experience such exchanges located mainly between W6-D11; N31-T43; N54-T72; M169-S176 of the fingers and between residues I77-V81 of the hand palm, including residue Q78 and T111-S130, covering the thumb region. All of these regions are spanning the binding cleft of the enzyme, including both the glycon (-1/-2/-3 subsites) and the aglycon (+1/+2/+3 subsites) sites (**Figure 4.9b**). A two-site exchange global fit of 30 dispersion profiles (R_{ex} > 2 s^{-1}) yielded a k_{ex} = 741 (±9) s^{-1} and an excited state fraction p_B= 9.2 (± 0.2) % (**Figure 4.4b**). The residues with enhanced R_{ex} are located in regions that experience conformational changes in the $(\mathbf{ES})_{open}$ compared to $\mathbf{E}_{free}$, as is revealed by the paramagnetic NMR study. For instance, the observed dynamics enhancement in the thumb regions is concomitant with pronounced ΔPCSs between the $(\mathbf{ES})_{open}$ to the $\mathbf{E}_{free}$ states. The same observation is for the fingers, hand palm and the α-helix (**Figure 4.9d**).

The binding of the substrate may enhance the exchange effects already observed for $\mathbf{E}_{free}$ by lowering the free energy of the excited state, thus increasing its population. This is in line with the observations for the **EP** state (*vide infra*). Exchange effects could also be caused by the association and dissociation of the substrate and the underlying chemical shift perturbations of the $\mathbf{E}_{free}$ and $(\mathbf{ES})_{open}$ states, however at 20 mM X6, the k_{ex} for the primary and secondary binding sites are 1.3 and 5.7 $.10^4$ s^{-1}, respectively. Such fast binding and dissociation will affect the RD curves negligibly. It should be noted that the PCSs are an average of all conformations that exchange faster than determined by the size of PCSs expressed in rad s^{-1}. So, in principle, the observed ΔPCSs could represent the weighted average of the PCSs in the $(\mathbf{ES})_{open}$ ground and excited states. We believe that this cannot explain all the ΔPCSs because the excited state is populated for 9%, suggesting that the PCSs for 100% excited state would differ up to 2 ppm from the ground state. Such large differences seem unrealistic.

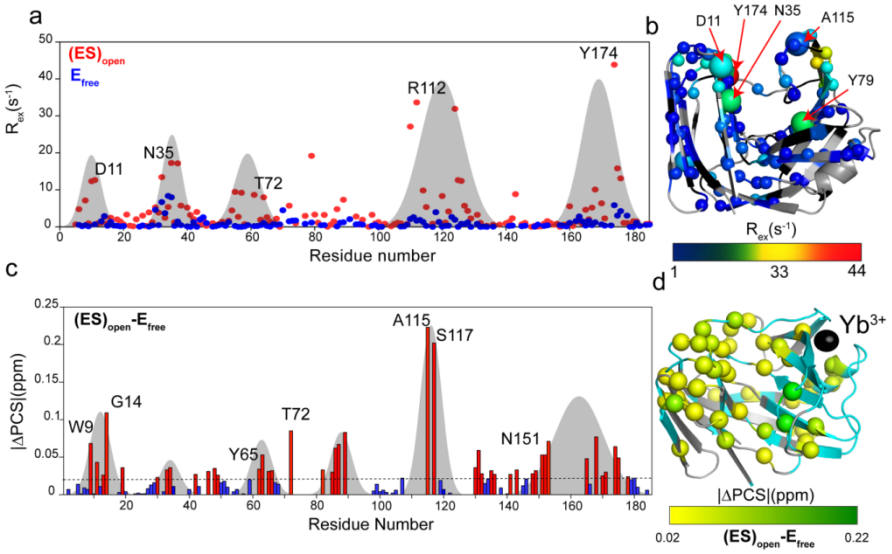

Figure 4.9. (**ES**)$_{open}$ **millisecond time scale dynamics**. (**a**) Overlay of the R_{ex} values of (**ES**)$_{open}$ (red circles) and BCX free states plotted versus the residue numbers. BCX regions that experience R_{ex} enhancements are highlighted with grey shade bell. (**b**) (**ES**)$_{open}$ complex R_{ex} values (> 1 s^{-1}) mapped on the BCX crystal structure (PDB ID: 1bcx). Backbone amides with moderate R_{ex} enhancement are shown in small spheres. Residues with a large enhancement are labelled and shown in big spheres. The residues are coloured based on their R_{ex} values by a blue/yellow/red gradient. (**c**) |ΔPCSs| between BCX free state and (**ES**)$_{open}$ states plotted versus the residue numbers to show the correlation between dynamics behaviour and PCSs changes in the (**ES**)$_{open}$ state. Outliers form the PCSs fit to the BCX crystal structure are shown in red bars. Protein regions with |ΔPCSs| > 0.02 ppm are highlighted with a grey shade bell. (**d**) |ΔPCSs| mapped on the BCX crystal structure. Residues with |ΔPCSs| > 0.02 are shown in spheres and coloured in yellow/green gradient indicating the strength of the |ΔPCSs|. Residues with |ΔPCSs| < 0.02 ppm are shown in grey cartoon and residues with non-determined |ΔPCSs| coloured in cyan. The black spheres indicate the position of the lanthanoid (Yb^{3+}).

BCX intermediate state (EI) conformation

Previously, the BCX intermediate state was trapped using a fluorinated substrate 2,4-dinitrophenyl-2-deoxy-2-fluoro-b-xylobioside (DNP-2FXb)[32,33]. The fluoride at the C2 position of the compound destabilizes the oxocarbenium transition state of the reaction, thus slowing the deglycosylation step and the good 2,4-dinitrophenolate leaving group warrants fast glycosylation of the enzyme. Therefore, the enzyme is trapped into its glycosylated form with a complex half-life of ~ 6 h at 40°C (**Figure 4.10a**). Here, an epoxide-xylobiose (epoxyX2) mechanism based inactivator was used to covalently trap the enzyme in its EI state. The inactivation mechanism involves the attack of the ligand epoxide active center by the enzyme nucleophile, resulting in ring opening and the formation of a covalent bond between the enzyme nucleophile and the inhibitor, which perfectly emulates **EI** state of the natural substrate hydrolysis reaction. The process is facilitated by protonation of the inactivator reactive center by the general acid/base

residue (**Figure 4.10b**). To generate the covalent complex, BCX was incubated with epoxyX2 at 1:20 ratio at 30°C. The reduction of BCX enzymatic activity was monitored over time using 4MU-xylobiose. After 4h of incubation no residual activity remained and the complex formation was identified by mass spectrometry after discarding the excess ligand by buffer exchange (**Figure 4.11a**). The complex was stable for months at room temperature. To investigate the binding site of the ligand within the protein binding cleft, a ^{15}N uniformly labelled sample of the **EI** was prepared for HSQC spectrum acquisition. By overlaying the **EI** with the protein free state spectrum $\mathbf{E}_{free}$ significant chemical shift perturbations were observed suggesting changes of the chemical environment of the backbone amides, either due to ligand binding or due to conformational changes experienced by the protein upon covalent complex formation (**Figure 4.11b**).

Due to these substantial chemical shift differences, it was difficult to accurately assign the **EI** spectrum only from the free enzyme peak list, so a ^{15}N ^{13}C double labelled **EI** sample was prepared and used for triple resonance experiments for backbone assignment. In the **EI** spectrum three residues were missing, presumably due to peak broadening, including E78, which is supposed to covalently bind to the C1 of the ligand, G70 and S117, which are in contact with the -1 subsite xylobiose sugar unit, according to BCX-2FXb crystal structure (PDB ID: 1bcx)[32]. The $\Delta\delta_{avg}$ between the $\mathbf{E}_{free}$ and **EI** states are plotted as function of the residue numbers in **Figure 4.12a**. Several clusters of amides show pronounced chemical shift perturbations between 0.1 and 0.6 ppm. Mapping the $\Delta\delta_{avg}$ on the protein crystal structure (**Figure 4.12b**) revealed that all of the observed perturbations are located within the protein binding site cleft, in the fingers and the thumb regions. The most significantly shifted residues are Y79, Y80 and V81, in the vicinity of the catalytic nucleophile E78 and also residues G173, Y174 and Q175, close to the catalytic acid/base E172. These observations point toward a correct covalent modification of the protein E78 nucleophile by the ligand and its correct positioning within the enzyme binding site. Although the ligand is supposed to only occupy the -1/ -2 subsites of the enzyme binding cleft, chemical shift perturbations were also observed in the +1/ +2 subsites. The distal chemical shift perturbations suggest changes in the protein conformation upon **EI** complex formation. To establish the presence of conformational changes in BCX upon formation of the **EI** state, diamagnetic and paramagnetic uniformly ^{15}N labelled samples of the **EI** complex were prepared using the procedure described above and 122 PCSs were obtained. To be consistent with the analysis of the $(\mathbf{ES})_{open}$ state, the observed PCSs of the **EI** were compared to the PCSs predicted from BCX crystal structure (PDB ID:1bcx) using the tensor parameters of the $\mathbf{E}_{free}$. Multiple outliers were observed suggesting that the crystal structure is not a good representation of the epoxyX2 structure in solution (**Figure 4.12e**). Most of the backbone amides PCSs, especially the ones in the fingers regions, are well correlated with the back-calculated PCSs from the protein crystal structure. Eighteen outliers were observed, mainly located

within the thumb region (**Figure 4.12f**). This suggests a different conformation of the thumb region in the **EI** solution state compared to its crystalline state.

The differences between the observed PCSs of the **EI** complex and $\mathbf{E}_{free}$ state (|ΔPCSs|) indicate also structural changes between the two states of the enzyme in solution (**Figure 4.12c**). The major |ΔPCSs| (≥ 0.02 ppm) are located within the enzyme binding cleft, the thumb and the finger regions, in addition to the C-terminal side of the α-helix (**Figure 4.12d**). For instance, residues G70, W71 and T72 and D119 show remarkable ΔPCSs. T72 is next to R73 which is connected to the tip the thumb region through a salt-bridge interaction with residue D119, therefore, it is plausible that any conformational changes experienced by the thumb results in effects on R73 and surrounding residues. Thus, these observations suggest that the thumb in the **EI** state adopts a different conformation than in the free state. W9 shows a ΔPCS of 0.07 which could stem from its different conformational when forming a CH-π stacking interaction with the ligand sugar ring at the -2 subsite, as revealed from the BCX-2FXb crystal structure[32]. The other residues are in close proximity to E78, which forms a covalent bond with the ligand. Residues T171 and Y174 located in the fingers regions of the +1/ +2 subsites also seem to experience structural changes in the **EI** state, being close to E172 acid/base residue. Correlations between ΔPCSs and $\Delta\delta_{avg}$ are observed suggesting the simultaneous contributions of ligand binding and its induced conformational changes on the protein structure into the significant differences between the **EI** and the $\mathbf{E}_{free}$ HSQCs spectra (**Figure 4.12a,c**).

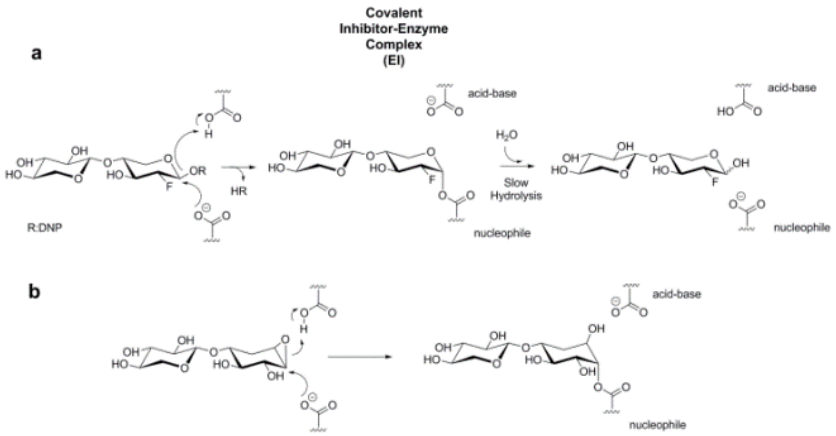

Figure 4.10. EI covalent complex formation by the DNP-2FXb (**a**) and the epoxyX2 (**b**).

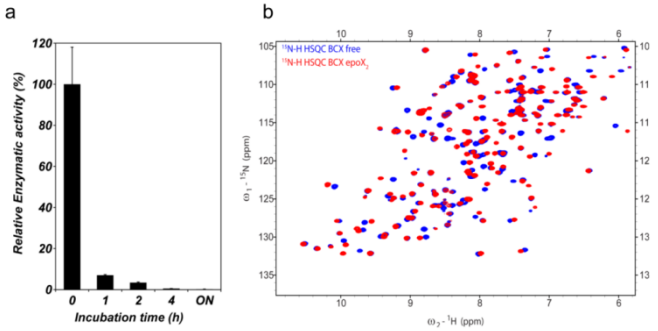

Figure 4.11. BCX-epoxyX2 complex formation. (**a**) Residual BCX activity monitored over course of incubation at 30 °C in the presence of 1:20 (BCX: epoxyX2) ratio. Error bars indicate ±SD of a duplicate. (**b**) ^{1}H-^{15}N HSQC spectra overlay of the $\mathbf{E}_{free}$ and **EI** states.

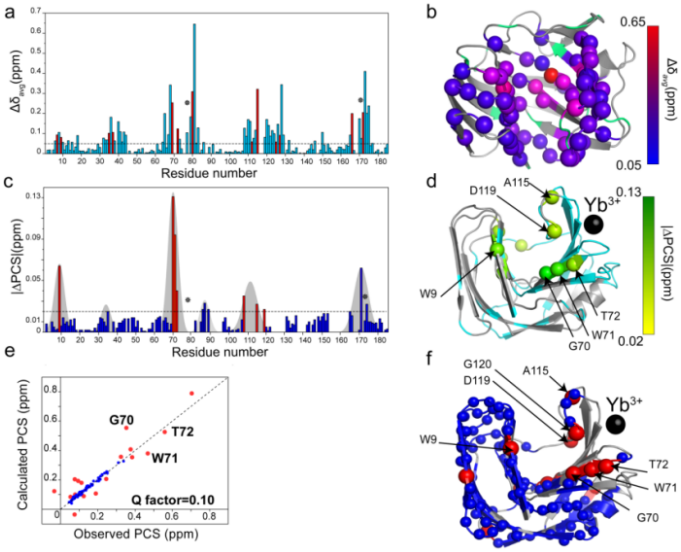

Figure 4.12. The BCX-epoxyX2 complex (**EI**). (**a**) $\Delta\delta_{avg}$ plotted versus BCX residue numbers. Residues that have direct interactions with the ligand (according to BCX crystal structure PDB ID: 1bcx) are shown in red bars. The positions of the E78/E172 catalytic dyad are market with asterisks. (**b**) Amino acid residues with $\Delta\delta_{avg} > 0.05$ ppm mapped on the BCX crystal structure (PDB ID: 1bcx) and coloured with a blue/red gradient. Residues with $\Delta\delta_{avg} < 0.05$ are shown in grey cartoon and the ones with non-determined $\Delta\delta_{avg}$ in green cartoon. (**c**) |ΔPCSs| plotted versus the residue numbers. Outliers of the PCSs fit to the BCX crystal structure are shown in red bars. The positions of the catalytic dyad are marked with asterisks. Protein regions with |ΔPCSs| > 0.02 ppm are highlighted with a grey shade bell. (**d**) |ΔPCSs| mapped on the BCX crystal structure. Residues with |ΔPCS| > 0.02 are shown in spheres and coloured by a yellow/green gradient based on |ΔPCSs| strength. Residues with |ΔPCSs| < 0.02 are shown in grey cartoon and the ones with non-observed |ΔPCSs| in cyan cartoon. The black sphere indicates the position of the lanthanide (Yb^{3+}). (**e**) Plot of the observed **EI** PCSs vs. calculated PCSs after fitting to the BCX crystal structure (PDB ID:1bcx) using $\mathbf{E}_{free}$ tensor parameters. Blue circles indicate PCSs with a deviation < 0.02 and red circles indicate PCSs of outliers (PCS deviation > 0.02). (**f**) **EI** observed PCSs mapped on the BCX crystal structure. Blue spheres indicate residues with the good correlation between experimental and predicted PCSs and red spheres indicate the outliers. Amides with non-observed PCSs are shown in grey cartoon.

EI dynamics

The previous study of the **EI** dynamics was performed for the ns to ps time scale, revealing no major changes of the dynamics on the probed time scales compared to its free state[33]. Here, the ms time scale chemical exchange of **EI** was probed by performing a CPMG RD experiment. Thirty-one residues show dispersion profiles ($R_{ex} \geq 1\ s^{-1}$), and these are located within the fingers region at the -1/ -2 subsites of the binding cleft in the proximity of the acid/base catalytic residue and the E78 nucleophile covalently bound to the ligand (**Figure 4.13a,b**). No chemical exchange was observed in the thumb region. The global fit of 15 residues with a $R_{ex} \geq 1.8\ s^{-1}$ revealed a $k_{ex} = 2.05\ (\pm\ 0.08) \times 10^3\ s^{-1}$ and an excited state fraction p_B of 0.6% (**Figure 4.4c**). A few residues show dynamic enhancement compared to the $\mathbf{E}_{free}$ as can be seen from the R_{ex} comparison between the two states (**Figure 4.13a**). The most pronounced changes are for residues I77, R112, T123 and T124, which are located in the vicinity of E78 and for residue G173, located next to E172, the acid base in the -1 subsites. A lesser R_{ex} increase is observed for residues W9, D11, G13 and G14, located in the -2 subsites in direct contact with the non-reducing end sugar ring of the ligand (**Figure 4.13c**). Concomitantly, residues T72, R73 and S74, located in a loop that connects the tip of the thumb to β-strands 6 and 7, show a reduction of their chemical exchanges, presumably as a result of the decrease of the thumb motion by ligand binding. Those residues also experience local conformational changes as concluded from their ΔPCSs (see above). As a conclusion, in the **EI** state the protein does not experience global dynamics changes, but it seems to assume local conformational changes, mainly located inthe fingers and the thumb at the aglycon binding site, where the ligand is covalently bound. However, few local chemical exchange enhancements were observed for residues surrounding the nucleophile and acid/base catalytic dyad presumably as a result of the covalent ligand binding. A slight reduction of the thumb and its surrounding loops in the ms time scale motion is noticed compared to $\mathbf{E}_{free}$ in solution (**Figure 4.13c**). The ms dynamics and PCSs studies suggest a different **EI** in solution average structure with local changes of the protein dynamics behaviour compared to the free state.

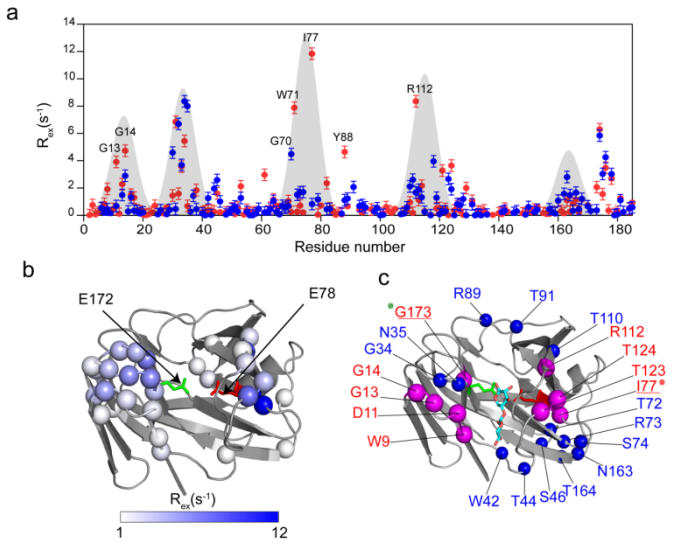

Figure 4.13. EI millisecond time scale dynamics. (**a**) Overlay between the R_{ex} values of the **EI** complex state (red circles) and $\mathbf{E}_{free}$ state plotted against the residue numbers. Regions that show differences of R_{ex} between the two states are highlighted with a grey shade bells. (**b**) **EI** complex R_{ex} values (> 1 s^{-1}) mapped in spheres on the BCX crystal structure (PDB ID: 1bcx) and coloured in a white/blue gradient. Residues with R_{ex} < 1 s^{-1} are shown in grey cartoon. E172 and E78 are shown in sticks and coloured in green and red, respectively. (**c**) Residues that show an R_{ex} enhancement or reduction in the **EI** state are mapped on BCX crystal structure (PDB ID:1bcx) and shown in pink and blue spheres, respectively. The catalytic dyad E78 and E172 are displayed in stick and coloured in red and green, respectively. Residues in the proximity of the catalytic dyad are indicated in asterisks. The DNP-2FXb ligand of BCX crystal structure is displayed in sticks[32].

BCX product (EP) complex conformation

The last step of xylanases enzymatic reaction is the product release from the -1/-2 /-3 subsites of the enzyme binding cleft. The binding mode of the product X2 in BCX cleft was monitored by an NMR titration using 1.3 mM, 13 mM, 65 mM and 130 mM ligand concentrations. The observed $\Delta\delta_{avg}$ are in the fast exchange regime, exhibiting progressive chemical shift changes. In contrast to the **ES** state, neither line broadening nor the appearance of secondary peaks was observed at high substrate concentration. Residues in the vicinity of the nucleophile and acid/base catalytic dyad at the -1/-2 subsites show significant $\Delta\delta_{avg}$, (**Figure 4.14a**). However, residues of the +1/+2 subsites do not show any chemical shift changes, which suggests differences in the binding affinity between the glycon and aglycon subsites. Substantial chemical shift changes (> 0.1 ppm) were observed for residues of the thumb regions, for instance S117 and D119 and for residues T69 and V37 located near the E78 and E172 catalytic dyad, respectively (**Figure 4.14b**). In addition, residues V168 and M169 positioned deep in the middle of the hand palm, approximately 10 Å distant from the catalytic dyad experience also significant $\Delta\delta_{avg}$.

The peak shape analysis of the HSQC spectra confirmed the absence of large peak broadening and revealed a dissociation constant of 10 mM and a k_{off}= 3.1(± 0.2) × 10^3 s^{-1}. Next, the local conformational changes of BCX upon ligand association were

investigated. Using the procedure described above, the changes in PCSs in every titration point were followed. The observed PCSs of the **EP** were compared to the PCSs predicted from BCX crystal structure (PDB ID:2bvv) using the tensor parameters of the $\mathbf{E}_{free}$ state in line with the analysis of the PCSs of the other states. The majority of the 125 PCSs correlate well with the predicted ones (Q = 0.077) with a few outliers located in the thumb loop (A115, S117, D119 and R122) (**Figure 4.14c,d**). The |ΔPCSs| between the free and **EP** states are plotted in **Figure 4.15C**. |ΔPCSs| showed dependence on ligand concentration and the subtle structural changes upon ligand binding occur in the thumb and the α-helix (**Figure 4.15c,d**).

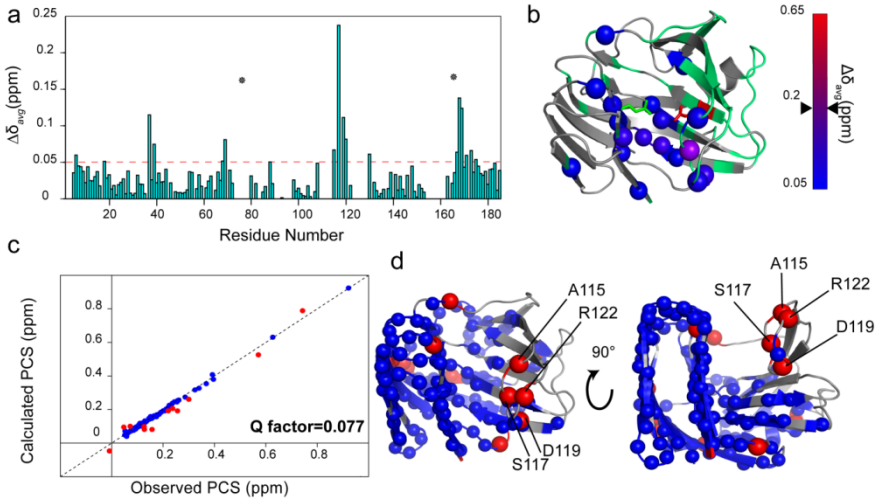

Figure 4.14. **The EP complex.** (**a**) $\Delta\delta_{avg}$ plotted against BCX residues numbers. Positions of the E78/E172 catalytic dyad are indicated with asterisks. (**b**) Residues with $\Delta\delta_{avg}$ > 0.05 ppm are mapped on the BCX crystal structure (PDB ID:2bvv) in spheres and coloured with a blue/red gradient using the maximum $\Delta\delta_{avg}$ value observed in the EI state as a colour gradient threshold for comparison. The colour gradient position of the maximum $\Delta\delta_{avg}$ (0.2 ppm) in the **EP** state is indicated by triangles. Amide residues with $\Delta\delta_{avg}$ <0.05 ppm are displayed in grey cartoon and the amides with non-determined $\Delta\delta_{avg}$ in green cartoon. (**c**) Observed PCSs vs. calculated of the **EP** state after fitting to the BCX crystal structure (PDB ID:2bvv). Blue circles indicate good correlation between the observed PCSs and the back-calculated ones. Red circles indicate outliers (>0.02). (**d**) **EP** observed PCSs mapped on the BCX crystal structure. Blue spheres indicate the positions of residues with good correlation between their observed PCSs and calculated PCSs. Red spheres indicated the structural positions of the outliers. Only residues of the protein thumb regions are named.

EP dynamics on the millisecond time scale

The paramagnetic NMR analysis suggests that in the **EP** state the protein adopts a slightly different conformation compared to the free form. However, in the presence of 130 mM X2 the protein exhibits a remarkable enhancement of exchange (R_{ex} up to 31 s^{-1}) in regions located within and on both sides of the binding cleft. The R_{ex} of the $\mathbf{E}_{free}$ and **EP** states are plotted in **Figure 4.15a** for comparison. The most significantly affected regions are clustered approximately between residues N32-F36 ($7\ s^{-1} \leq R_{ex} \leq 31\ s^{-1}$), forming a loop that connects β-strands 3 and 4 in the -1 subsite of the fingers; between residues Y69-Y80 ($7\ s^{-1} \leq R_{ex} \leq 21\ s^{-1}$) in β-strands 7 and 8 of the palm, including the nucleophile E78; between R112-Q127 ($1.5\ s^{-1} \leq R_{ex} \leq 31\ s^{-1}$) that forms the thumb loop and between T171-S176 that accommodates the acid/base E172 (**Figure 4.15b**). Other residues remote from the active site (S140-T143, positioned on the non-catalytic side of the palm) experience smaller exchange effects. A global two-site exchange fit of 36 residues ($R_{ex} \geq 1.8\ s^{-1}$) yielded a $k_{ex} = 1.53\ (\pm 18) \times 10^3\ s^{-1}$ and an excited state population of 4% (**Figure 4.4**). The peaks shape analysis of BCX titration with 130 mM X2 (> 92% saturation) revealed a dissociation rate constant $k_{off} = 3.1\ (\pm 0.2) \times 10^3\ s^{-1}$ (see above). At 92% saturation, k_{ex} can be calculated to be $3.9 \times 10^4\ s^{-1}$, which is outside the range of CPMG RD time window. Therefore, its is assumed that the observed enhancement of the protein amide chemical exchange is dominated by structural fluctuations in the **EP** state rather than ligand dissociation. Interestingly, residues like G70 and R112 in the vicinity of E78 and residues N35 and S117 of the fingers and the thumb loop, respectively, show a distinctive increase of their dispersion profiles compared to the free state. N35 and S117 resides on the top of both side of the binding cleft, separated by ~12 Å distance (**Figure 4.15b**). The tremendous enhancement of their R_{ex} might reflect their involvement in the structural fluctuation of the binding cleft width while the ligand is associated to the protein. Additionally, regions that experience changes of their dynamics properties are also involved in conformational changes in the **EP** state as suggested by $\Delta\delta_{avg}$ and ΔPCSs (**Figure 4.15c,d**).

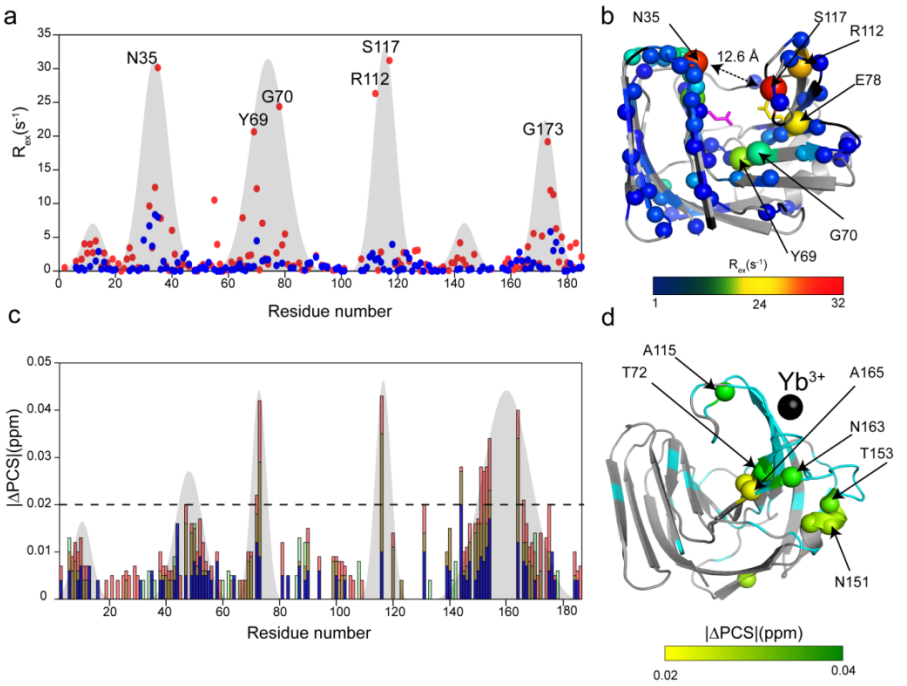

Figure 4.15. EP millisecond time scale dynamics. (**a**) Overlay between the R_{ex} values of **EP** complex state (red circles) and the BCX free state plotted against the residue numbers. BCX regions that experience Rex enhancements are highlighted with grey rectangles. (**b**) **EP** complex R_{ex} values (> 1 s^{-1}) mapped on the BCX crystal structure (PDB ID: 1bcx). Residues with moderate R_{ex} enhancement are shown in small spheres. Residues with a remarkable enhancement are shown in big spheres. The residues are coloured based on their R_{ex} values by a blue/yellow/red gradient. (**c**) |ΔPCSs| between the **EP** and $\mathbf{E}_{free}$ states plotted against the residue numbers. |ΔPCSs| in the presence of 13 mM X2 are displayed in blue bars; the ones in the presence of 65 mM X2 are displayed in green bars and the ones in the presence of 130 mM X2 are in red bars. Protein regions that show ligand dependency of their |ΔPCSs| are highlighted in grey shade bell. (**d**) Amino acid residues with |ΔPCSs| > 0.02 ppm are shown in spheres on the BCX crystal structure (PDB ID: 2bvv) and coloured with a yellow/green gradient. Residues with |ΔPCSs| < 0.02 are displayed in grey cartoon and the ones with non-determined |ΔPCSs| are shown in cyan cartoon. The black sphere indicates the position of the lanthanide (Yb^{3+}).

Discussion

BCX substrate binding modes and conformational landscape during catalysis

To investigate BCX substrate binding mechanism and follow its conformational changes during catalysis ^{1}H-^{15}N HSQC NMR titrations and PCSs were used. Together, these approaches provided detailed information about the substrate binding site location and the binding kinetics in conjunction with indications of conformational changes during the enzyme catalytic pathway.

The fit of the experimental PCSs for free BCX to the protein crystal structure (PDB ID:2bvv)[32] revealed a good agreement between the solution and crystalline ground states. Second, the binding kinetics of BCX to a substrate (X6, **ES** complex) was examined by NMR titration. For this purpose, the E78 nucleophile of the enzyme was substituted for Q, abolishing catalytic activity. During the course of titration, a complex chemical shift perturbation pattern of the backbone amide groups was observed concomitant with general line broadening. This effect was attributed to an increased viscosity caused by the xylose oligosaccharides. Viscosity determine the rotational diffusion time and thus relaxation rates of the protein. Similar observations were made in previous reports[34]. Chemical shifts changes in the fast exchange regime were noticed for the amides that form the secondary binding site[34]. Interestingly, at a X6 concentration at which BCX is partially saturated, new secondary peaks emerged for multiple backbone amides located within the binding cleft and its surrounding, indicating the existence of two **ES** bound states. The line shape analysis of the peaks showing this behaviour is suggests an "induced fit" binding mechanism. Therefore, it is hypothesised that in the **ES** state the substrate first binds to the protein in an open form $(\mathbf{ES})_{open}$ inducing a global closure of its binding cleft $(\mathbf{ES})_{closed}$. The exchange rate of this process is 20 s^{-1}, which coincides with the hydrolysis rate of BCX artificial substrate PNP-X2, therefore the open and close motion of the protein binding cleft might play a role in substrate turnover[36].

To interrogate the different conformations of the **ES** state, the PCSs of the $(\mathbf{ES})_{open}$ and $(\mathbf{ES})_{closed}$ complexes were measured. The PCSs fit of $(\mathbf{ES})_{open}$ to the BCX crystal structure (PDB ID: 2bvv) shows multiple outliers located within the binding cleft especially for residues that form the thumb, fingers and the α-helix and including also residues in the middle of the hand-palm. The PCSs differences between the free and the $(\mathbf{ES})_{open}$ revealed further conformational changes of the protein on both sides of the catalytic cleft, including residues that form the β-strands A and B. Thus, it was concluded that the $(\mathbf{ES})_{open}$ conformation is different from the one observed in the free protein. Those pronounce conformational changes of the protein structure might be consequence of simultaneous binding of the substrate in the aglycon and glycon subsites because such large effects are not observed when titrating with X2 (see below). Additionally, the few PCSs measured for residues that exhibit a resonance in the $(\mathbf{ES})_{closed}$ state included three amides that do not correlate well with their PCSs in the $(\mathbf{ES})_{open}$ state. Those amino acid residues were located in the thumb and deep in the hand palm. Therefore, it is concluded that substrate binding in the **ES** state follows an induced fit mechanism, which provoke two-bound states, none of them resemble the free state conformation of the protein. Previous studies on GH11 xylanases titration with oligosaccharides did not report the same observations[30, 34]. The structure obtained by co-crystallization of a silenced variant of GH11 xylanase from *Trichoderma reesei* with X6 shows a movement of the thumb region toward the ligand (2 Å compared to the free protein) enabling the formation of close interactions with xylose subunits at the -1/-2/-3 subsites[37]. This thumb motion might occur in the BCX **ES**

complex in solution, although it is assumed that these local conformational changes in the thumb may not explain the observed global conformational changes of the binding cleft in the $(\mathbf{ES})_{open}$ state, as suggested by PCSs.

The next step was to characterize the enzyme in the intermediate state of the reaction (**EI**) by using an epoxy-xylobiose (epoxyX2) compound, which forms an adduct to the enzyme. CSPs were not only observed for residues at the -1/-2, subsites, including the thumb and the fingers, but also for distal residues in the aglycon pocket, suggesting the occurrence of a conformational change upon adduct formation. The **EI** PCSs fits to the **EI** crystal structure (PDB ID:1bcx) revealed multiple outliers for amides located mostly in the thumb region an indication for a different conformation in solution.

The map of |ΔPCSs| between the **EI** and $\mathbf{E}_{free}$ states showed that residues involved in direct interactions with the ligand experience the most significant conformational changes. Therefore, both the thumb and residues at the -1/-2 subsites seem to adopt a new conformation when the protein is covalently bound to the ligand.

In the **EI** complex an outward displacement of thumb was observed in XynII crystallized with epoxyalkyl xylobiosides [38] and also a 1.1 Å thumb displacement was observed in the BCX crystal structure when bound to the 2FXb compared to its free form[32]. Nevertheless, the fit of the **EI** PCSs to the BCX intermediate-state structure did not show a good correlation, suggesting that the **EI** adopts a conformation in solution that differs from the one in the crystal.

The last step of the reaction is the product release from the glycon pocket. Studying the chemical shift perturbations upon protein titration with X2 revealed a ligand binding in the fast exchange regime with $k_{off} = 3.1\ (\pm 0.2) \times 10^3\ s^{-1}$. No minor peaks were observed at high product concertation, contrary to the titration with X6. The ligand seems to occupy only the -1/-2 subsites not the +1/+2 subsites. This suggests a difference in the binding sites affinities between the glycon and aglycon sites towards the product. These differences in affinity might be an adopted mechanism by the enzyme to facilitate the dissociation of the leaving group from the aglycon site. The paramagnetic NMR experiments on the **EP** complex revealed that the **EP** complex structure exhibits only small deviations from the $\mathbf{E}_{free}$ crystalline state, localized in the glycon site, in the thumb (-1/-2 subsite) and the α-helix.

The **EP** complex has been trapped by co-crystallizing a GH11 xylanase from *Trichoderma reesei* with X6 due to the substantial reduction of its catalytic activity by single point mutation. The only significant conformational changes of the protein in the **EP** complex were observed in the thumb region where the atoms move closer to the product compared to their position in the ligand free structure of the mutant[37].

Therefore, based on crystallography studies of GH11 xylanases in complex with covalent and non-covalent ligands, the thumb region of the β-jelly roll fold might experience two types of movement: a movement that brings the thumb closer to the substrate in the case of non-covalent ligands, while in the **EI** complex the thumb experiences a backward

movement, which seems to assist the accommodation of the covalent ligands into the -1/-2 subsites. It is speculated that the modulation of the thumb region conformations by the covalent and the non-covalent forms might play a role in positioning the substrate into the correct configuration to facilitate the glycosidic link hydrolysis and also to assist the product release from binding cleft in the final step of the catalytic reaction.

This study of BCX covalently and non-covalently bound to its ligands revealed conformational changes not only of the thumb region but also within the α-helix and its binding cleft. The conformational changes depend also on the length of the bound substrate and on the occupancy of the protein glycon and aglycon sites.

BCX dynamics during catalysis

After studying the different average conformations of the protein in each step of its catalytic cycle, it was aimed to follow the ms time scale motions to investigate if there is an interconnection through their sampled excited states. The enzyme in the free state shows small chemical exchange effects for residues located mainly within the finger and the thumb regions. A two-site exchange model fit of the dispersion data revealed a k_{ex}= 2.5×10^3 s^{-1} and a population of the excited state p_B of 0.7%. The global rate of xylanase B2 (XlnB2) from *Streptomyces lividans* conformational exchange is equal to $k_{ex} = 1.2 \times 10^3$ s^{-1} for several residues in the fingers, yet no chemical exchange was observed in the thumb[30].

Next, the dynamics behaviour of the enzyme in the $(\mathbf{ES})_{open}$ state was examined by using a silenced version of the enzyme in the presence of X6 as a substrate. A global ms time motion enhancement was observed with a prominent increase of the R_{ex} (up to 50 s^{-1}). Amino acid residues that sculpture the binding cleft in addition to residues remote from the binding site experienced exchange.

Residues with enhanced R_{ex} exchange were also identified to experience conformational changes in the $(\mathbf{ES})_{open}$ upon ligand binding. The calculated k_{ex} of the substrate binding in the binding cleft and secondary binding site are 1.3 and 5.7×10^4 s^{-1} respectively, which falls outside the time scale window of the CPMG RD experiment. Therefore, the contributions of the dissociation process to the RD are considered negligible and the observed ms motion enhancement seems to be dominated by the intrinsic structural fluctuations of the protein in the $(\mathbf{ES})_{open}$ state.

The enhancement of the ms time scale dynamics was also observed in the case of XlnB2 in the presence of xylopentaose with an increase in its global k_{ex} from 1.2×10^3 s^{-1} to 3×10^3 s^{-1}. Residues of the fingers region, hand palm and thumb showed significant conformational exchanges leading to the conclusion that the substrate triggers the ms motion of the protein especially in the thumb, which was observed to be rigid in the free state[30]. However, in BCX, substrate binding reduces the k_{ex} from 2.5×10^3 s^{-1} in the free state to 740 s^{-1} in the $(\mathbf{ES})_{open}$ complex. The explanation for the different substrate effects

between the two homologues (40% primary sequence identity) of GH11 xylanases is unclear.

The **EI** complex experiences subtle dynamics changes compared to the free protein with k_{ex}= 2 (±0.08) × 10^3 s^{-1} and p_B= 0.6 %, when fitted to a global two-site exchange model. Nonetheless, local chemical exchange enhancement of residues in the vicinity of the catalytic dyad were observed, concomitant with a reduction of the thumb region dynamics and its surrounding loops, presumably due to the covalent ligand binding.

The last step of the reaction is the product dissociation from the enzyme binding site. By following the dynamic of the **EP** state, a pronounced enhancement of the ms time scale chemical exchange was observed although to a lesser degree than in the ES complex. Significant R_{ex} increases were noticed for amides of the thumb and the fingers at the -1/-2 subsites. The global fit of the dispersion profile to a two-site exchange model revealed a k_{ex}=1.5 × 10^3 s^{-1} and 4% of the protein in the excited state. The observed increase of the protein dynamics is not related to $\Delta\delta_{avg}$ caused by ligand binding (k_{ex}= 3.9 × 10^4 s^{-1}).

All of the mentioned observations indicate a diversity in the protein dynamics behaviour in each step of the catalytic cycle, which depends on the substrate mode of binding (covalent or non-covalent) and also on its length (number of sugars units). To unravel the conformational connections between the BCX ground states, a comparison between the $\Delta\delta_N$ and the $\Delta\omega_N$ from the global CPMG RD data fits was performed. No correlations between the $\Delta\omega_N$ values of the $\mathbf{E}_{free}$ and **EI** excited states with the $\Delta\delta_N$ of the $(\mathbf{ES})_{open}$ and the **EP** were observed, suggesting that those excited states are not interconnected (**Figure 4.16a,b**). A correlation was observed, however, between $\Delta\omega_N$ values of $(\mathbf{ES})_{open}$ excited state and the $\Delta\delta_N$ of the **EI** ground state (**Figure 4.17a**). For instance, residues N114, F125, T126, Q127 and Y128, clustered in the thumb region, show a remarkable correlation with a R^2=0.8 (**Figure 4.17c**). Additionally, Y79, located next to E78 that form a covalent bond with the ligand in the **EI** state, show also a strong correlation. These observations suggest that the conformation of the thumb and residues proximal to the nucleophile in the $(\mathbf{ES})_{open}$ excited state resemble the adopted conformation in the **EI** ground state. Similarly, a correlation between the **EP** excited and **EI** ground states is observed, for residues I77, Y79 and Y80 in close proximity of the E78 nucleophile in conjunction to N114 and T126 of the thumb region (**Figure 4.17b,d**). This suggests that also the **EP** complex visits the **EI** conformation. Based on these observations, it is proposed that the $(\mathbf{ES})_{open}$ and **EP** ground states are connected through an excited state conformation in which the thumb and the proximal residues of the nucleophile adopt a conformation that resembles the one observed in the **EI** ground state.

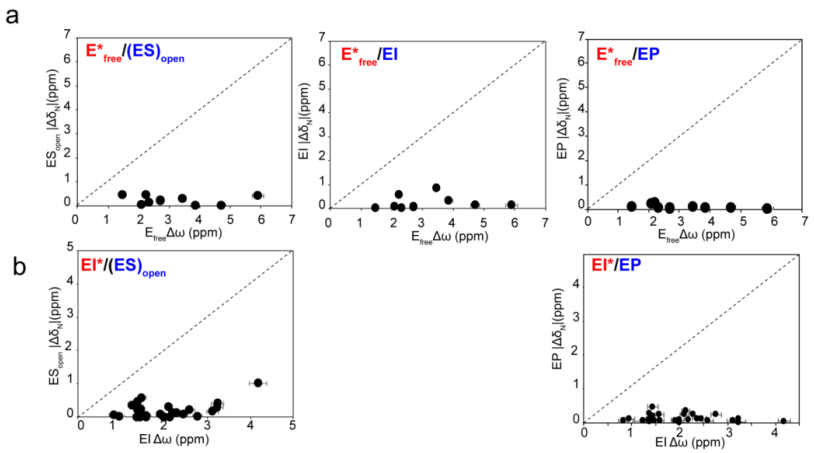

Figure 4.16. Correlation between the Δω from global residues fits of the CPMG RD data with the $\Delta\delta_N$ of the NMR titration data. (**a**) The Δω of the $\mathbf{E}_{free}$ excited state plotted against the $\Delta\delta_N$ of the $(\mathbf{ES})_{open}$, **EI** and **EP** ground states. (**b**) The Δω of the **EI** excited state plotted against the $\Delta\delta_N$ of the $(\mathbf{ES})_{open}$ and **EP** ground states. Excited states are indicated in red and marked with asterisks and ground states in blue.

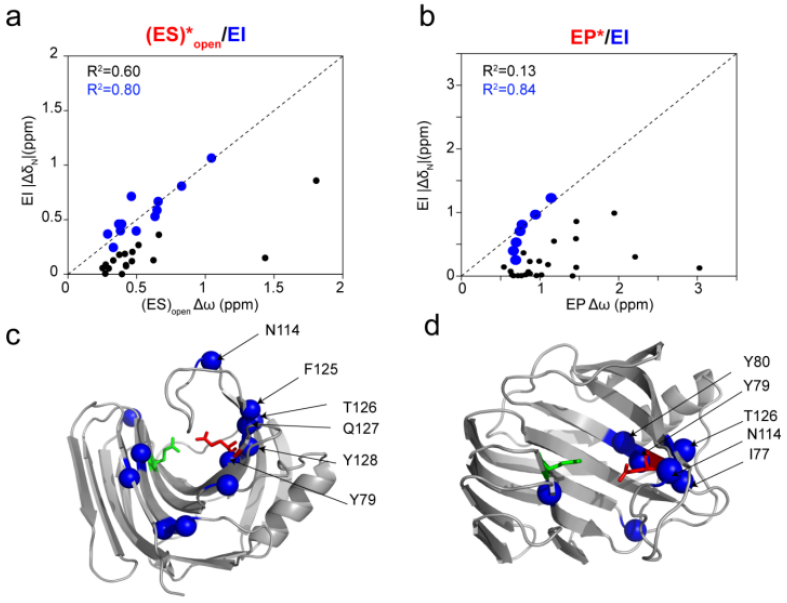

Figure 4.17. Correlation between excited states and the **EI** ground state. (**a, b**) Correlation of Δω of the $(\mathbf{ES})_{open}$ excited state (**a**) and the **EP** excited state (**b**) with the $\Delta\delta_N$ of **EI** state. Good correlations are shown in blue circles and the poor ones in black dots. The correlation factor (R^2) is indicated using the same colour code. (**c, d**) Backbone amides that show a good correlation for $(\mathbf{ES})_{open}$ (**c**) and **EP** (**D**) excited state chemical shifts with **EI** ground state chemical shifts are mapped on the BCX crystal structure (PDB ID:2bvv) in blue spheres. Some residues are labelled. Acid/base and nucleophilic catalytic residues are shown in green and red, respectively.

Conclusions

The aim of this study was to follow the conformational changes and dynamics of GH11 xylanase during their catalytic pathway, using BCX as a model. The titration and paramagnetic NMR experiments identified different binding modes of the enzymes to its substrate and product, which seems to be concomitant with changes of the protein conformation. The conformational changes are dependent on the mode of the ligand interactions (non-covalent versus covalent) and also on the glycon and aglycon binding sites occupancy.

MD simulations by Muilu et al. on XYNII from *Trichoderma reesei,* captured in different crystalline states, suggested that the protein samples three sequential substates during its catalytic reaction. First, the protein adopts an open state to accommodate the substrate in the cleft. Substrate binding induces a closed conformation necessary for positioning the substrate into the correct configuration for glycosidic bond hydrolysis. The last state is a loose structure from which the product is released[91]. The results of MD simulations are in agreement with the present study in the solution state. Nevertheless, BCX seems to display more diverse conformational and dynamics behaviour during its catalytic pathway. Therefore, a new model is proposed for the GH11 xylanase conformational landscape changes and the contribution of dynamics to catalysis.

PCSs analysis showed that the protein adopts at least five distinctive average structures where approximately five regions, including the fingers, the hand palm, the thumb, the cord and the α-helix contribute to this conformer diversity. The protein in the free state ($\mathbf{E}_{free}$) is in an open structure. The NMR titration of BCX with substrate point toward an induced fit binding mechanism, suggesting that the protein indeed experiences conformational changes necessary for the formation of the Michaelis complex. Based on the chemical shifts and the PCSs, it was concluded that the two **ES** bound states conformations differ from each other as well as from that of the free state. The induced state seems to be similar to the $(\mathbf{ES})_{closed}$ state, yet is formed slowly, indicating a high activation barrier for its formation. It may be the dual occupancy of the glycon and the aglycon sites that induces this rearrangement. The slow conversion could limit catalysis, as the rate of formation is of a similar size as the turnover rate. The observed ms enhancement of the $(\mathbf{ES})_{open}$ motion in residues that sculpture the binding cleft, including the thumb and the fingers, could be an indication of structural fluctuations necessary for substrate positioning, deformation or even sliding, a process that was observed in other biomass degrading enzymes like cellulases[39]. Through the $(\mathbf{ES})_{closed}$ state, the glycosylation step occurs and the protein is locked into a closed conformation $(\mathbf{EI})_{closed*}$ that differs from the $\mathbf{E}_{free}$, $(\mathbf{ES})_{open}$ and $(\mathbf{ES})_{closed}$ ground state conformations. The covalent bond formation restricts the protein dynamics in the thumb region concomitant with an observed enhancement of the ms motion for residues surrounding the nucleophile. Those subtle

dynamics enhancement may play a role in the hydrolysis of the glycosidic bond of the glycosyl-enzyme by the activated water molecule. Through the **EI** ground state, the deglycosylation takes place and the protein adopts a loose conformation $(\mathbf{EP})_{loose}$. The remarkable enhancement of the ms protein motion between the **EP** and the **EI** ground states (between loose and closed conformations) may play a role in triggering the product release from the glycon site of the enzyme binding cleft (**Figure 4.18**). In the $(\mathbf{ES})_{open}$ and **EP** state the protein samples an excited state conformation similar to the **EI** ground state. The amplitude and directions of those conformational changes remain unknown. The calculation of the structure of the **EI** complex using NMR spectroscopy is on-going. Solving the **EI** structure may assist the modelling of the protein conformations in the **EP** and **ES** states based on their experimental PCSs and by using the **EI** NOEs as additional structural restraints.

In this study, the aim was to shed light on the possible contributions of the conformational dynamics of GH11 xylanases to their paradigmatic hydrolysis mechanism.

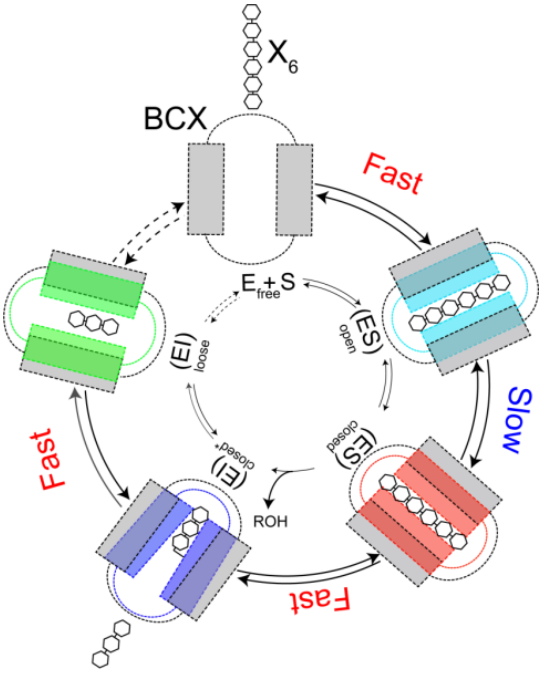

Figure 4.18. Conformational landscape of BCX during catalysis. The different schematic shapes and colours indicate different protein conformations and dynamic behaviour. Dashed arrows indicate non-probed conformational exchange between the different states.

Material and Methods

Mutagenesis

BCX E78Q, BCX T109C/T111C and BCX E78Q T109/T111C mutants were prepared by site-directed mutagenesis using Quik-Change protocol. The presence of the mutations was confirmed by sequencing.

BCX overexpression and NMR samples preparation

The gene of BCX with a sequence optimized for expression in *E. coli* was purchased from life technologies, including a N-terminus 6-His-Tag followed by a TEV protease recognition site. The gene was subcoloned into plasmid pET28a using NcoI/XhoI restriction sites. *E. coli* BL21DE Rosetta cells were transformed with the obtained vector and cultured in 2 ml lysogency broth media containing 100 μg/mL kanamycin for 6 hours at 37°C. 100 μl of the miniprep culture were used to inoculate 50 mL minimum medium supplemented with ^{15}N labeled ammonium chloride ($^{15}NH_4Cl$) or in combination with ^{13}C-glucose. The next day, 0.5 L of the same medium was inoculated with the overnight preinoculation culture and incubated for 8 hours at 37°C with shaking until the OD_{600} reached 0.6. BCX gene expression was induced with 0.5 mM IPTG and the culture was incubated overnight at 20°C with shaking. The cells were harvested by centrifugation and the pellet was resuspended in an extraction buffer (50 mM phosphate buffer solution (PBS), 40 mM imidazole, pH 7.5) and sonicated. The resulting 6His-BCX supernatant was purified by Ni(II) affinity chromatography. Subsequently, the eluted BCX fractions were collected and the protein was brought into a solution of 50 mM PBS using PD10 column. The 6-His-BCX protein was incubated with TEV protease overnight at 4°C. Next, the cleaved 6-His-Tag and the TEV protease were separated from BCX using Ni(II) affinity chromatography. The unbound protein fraction, that included BCX, was collected and buffer exchanged to 25 mM sodium acetate buffer pH= 5.8 using PD10 column. The protein was concentrated using Amicon® Ultra-Centrifugal Filters with 10 kDa cutoff and its purity was checked by SDS page. The BCX concentration was determined by UV absorbance using the theoretical extinction coefficient of 84,3 M^{-1} cm^{-1}.

EI covalent complex formation

The epoxyX2 was synthesized by Schroder S.P. et al.[40]. The protein was incubated with 20 times molar equivalent of BCX sample at 30 °C. The reduction of the enzyme activity was monitored over the course of incubation using 4MU-xylobiose as a substrate (Megazyme). The reaction rates were monitored by measuring the fluorescence of the released 4MU at its emission wavelength of 445 nm on a Cary Eclipse Fluorescence Spectrophotometer (Agilent). After an overnight incubation, the excess of epoxyX2 was removed using PD10 column and complex formation was checked by electrospray mass spectrometry (Waters). The same procedure was applied to prepare a ^{15}N ^{13}C BCX-epoxyX2 sample (for assignment), ^{15}N BCX-epoxyX2 sample (for ^{15}N CPMG RD) and ^{15}N BCX T109C/T111C-LaNP-5-(Lu^{3+}/Yb^{3+})-epoxyX2 samples for PCSs calculations.

NMR spectroscopy

Sequential assignment of the BCX WT at 20 °C was performed by recording triple resonance HNCACB and CBCAcoNH spectra on a ^{15}N ^{13}C BCX NMR sample (0.6 mM)[22]. The obtained peak list was used to assign the BCX E78Q, BCX T109C/111C and BCX E78Q T109C/111C mutants backbone amides. The assignments of these later were curated using PCSs. The same assignment procedure as for the BCX WT was applied for the assignment of the BCX-epoxyX2 (**EI** complex). The NMR spectra were acquired on Bruker Avance III (HD) 600 or 850 MHz spectrometers, equipped with TCI cryoprobes, processed by TopSpin 3.5 (Bruker Biospin) and analysed with Sparky Software[41].

NMR titration with oligosaccharides and peak shape analysis

The NMR titration of ^{15}N BCX E78Q (123 μM) with an increasing X6 concentration (123 μM-20 mM) was performed in 25 mM sodium acetate (pH=5.8) and 6% D_2O at 20 °C. The ^{1}H-^{15}N HSQC spectrum of every titration point was recorded and the average chemical shift perturbation values ($\Delta\delta_{avg}$) relative to the free protein were calculated according to the equation:

$$\Delta\delta_{avg}=\sqrt{\Delta\delta_H^2 + \frac{\Delta\delta_N^2}{25}}$$

An iterative least-squares procedure for 2D peak shape analysis of the HSQC titration spectra was performed using TITAN software[35] and the titration data were fitted to either a two-state or an induced fit binding model. The fit yielded the K_d and k_{off} values and also the R_2 relaxation, in addition to the k_{open} and k_{closed} for the induced fit binding model.

Paramagnetic NMR spectroscopy

Uniformly labelled ^{15}N BCX T109C/T111C was incubated with 10 mM DTT in 50 mM PBS (pH=7.2) and 150 mM NaCl for 1 h on ice to reduce the disulphide bridges between the protein dimers. DTT was removed by using a PD10 column. The protein was mixed with 10 molar equivalents of CLaNP-5-Lu^{3+} (diamagnetic sample) or CLaNP-5-Yb^{3+} (paramagnetic sample) and left stirring for 2 h at room temperature. The samples were concentrated to 0.5 mL using a 10 kDa Amicon® Ultra-Centrifugal Filter and injected into a Superdex G75 analytical gel filtration column to remove unreacted tag and protein dimers. To verify the labelling efficiency, the protein samples were analyzed on 15 % SDS-PAGE in the presence and absence of a reducing reagent (β-mercaptoethanol) and checked by acquiring ^{1}H-^{15}N HSQC spectra. weak peaks of untagged BCX were observed for both samples (<5% unlabeled). The obtained PCSs were fitted to the BCX crystal structures (PDB ID:2bvv or 1bcx) to optimize the location of the lathanoid and the tensor position and orientation using Numbat software[42]. The Q factor score of the experimental PCSs fit to the BCX crystal structure was calculated using the equation[43].

$$Q = \sqrt{\frac{\sum (obs - calc)^2}{\sum (obs + calc)^2}}$$

A jackknife error analysis of the obtained tensors is part of the Numbat software and was used to enable $\Delta\chi$ tensor comparison for different BCX states. The differences between the experimental PCSs of each BCX ligand-complex and the free protein were also calculated to monitor the conformational changes that occur upon ligand binding.

NMR relaxation dispersion and CPMG data analysis

^{15}N CPMG RD data sets were recorded at 20 °C using a ^{15}N TROSY-CPMG pulse scheme[44]. Data sets were recorded at field strengths of 11.7 T (600 MHz) and at 19.9 T (850 MHz). The constant time relaxation delay, τ_{CPMG}, was set to 50 ms. Dispersion profiles comprised ~ 20 different ν_{CPMG} frequencies, recorded in an interleaved manner, with values ranging from the minimum possible value ($1/\tau_{CPMG}$) to a maximum of 1000 Hz. Errors were estimated on the basis of repeat measurements at two or three different ν_{CPMG} frequencies. Each CPMG dataset required approximately 14 hours of measurement time. All experiments were performed on Bruker spectrometers equipped with a TCI-Z-GRAD triple resonance cryoprobe. The peak shape fit of the 3D-pseudo plans was performed using FuDa[45] .The $R_{2,eff}(\nu_{CPMG})$ were obtained via the relation:

$$R_{2,eff}(\nu_{CPMG}) = \frac{1}{T_{relax} \times \ln\left(\frac{I_{\nu_{CPMG}}}{I_0}\right)}$$

Where $I(\nu_{CPMG})$ and I_0 are peak intensities with and without the 50 ms τ_{CPMG}, respectively. Values of the exchange parameters were extracted from a global fit of $R_{2,eff}(\nu_{CPMG})$ profiles to a two-site exchange model using CATIA (http://www.biochem.ucl.ac.uk/hansen/catia). The experimental R_{ex} were calculated using the formula $R_{ex} = R_{2,eff\,(20\ Hz)} - R_{2,eff\,(1000\ Hz)}$ and plotted versus the residue numbers.

References

1. Wolynes, P. G. (2005) Recent successes of the energy landscape theory of protein folding and function, Q. Rev. Biophys. 38, 405-410.
2. Hegler, J. A., Weinkam, P., and Wolynes, P. G. (2008) The spectrum of biomolecular states and motions, HFSP journal 2, 307-313.
3. Mulder, F. A., Mittermaier, A., Hon, B., Dahlquist, F. W., and Kay, L. E. (2001) Studying excited states of proteins by NMR spectroscopy, Nat. Struct. Mol. Biol. 8, 932-935.
4. Söderberg, O., Gullberg, M., Jarvius, M., Ridderstråle, K., Leuchowius, K.-J., Jarvius, J., Wester, K., Hydbring, P., Bahram, F., and Larsson, L.-G. (2006) Direct observation of individual endogenous protein complexes in situ by proximity ligation, Nat. Methods 3, 995-1000.
5. Petersen, F. N. R., and Bohr, H. (2010) The mechanisms of excited states in enzymes, Theor. Chem. Acc. 125, 345-352.
6. Eisenmesser, E. Z., Bosco, D. A., Akke, M., and Kern, D. (2002) Enzyme dynamics during catalysis, Science 295, 1520-1523.
7. Nitsche, C., and Otting, G. (2016) Pseudocontact shifts in biomolecular NMR using paramagnetic metal tags, Prog. Nucl. Magn. Reson. Spectrosc.
8. Gaponenko, V., Sarma, S. P., Altieri, A. S., Horita, D. A., Li, J., and Byrd, R. A. (2004) Improving the accuracy of NMR structures of large proteins using pseudocontact shifts as long-range restraints, J. Biomol. NMR 28, 205-212.
9. Chen, J. L., Wang, X., Yang, F., Cao, C., Otting, G., and Su, X. C. (2016) 3D structure determination of an unstable transient enzyme intermediate by paramagnetic NMR spectroscopy, Angew. Chem. Int. Ed. 55, 13744-13748.
10. Keizers, P. H., Saragliadis, A., Hiruma, Y., Overhand, M., and Ubbink, M. (2008) Design, synthesis, and evaluation of a lanthanide chelating protein probe: CLaNP-5 yields predictable paramagnetic effects independent of environment, J. Am. Chem. Soc. 130, 14802-14812.
11. Meiboom, S., and Gill, D. (1958) Modified spin-echo method for measuring nuclear relaxation times, Rev. Sci. Instrum. 29, 688-691.
12. Carr, H. Y., and Purcell, E. M. (1954) Effects of diffusion on free precession in nuclear magnetic resonance experiments, Phys. Rev. 94, 630.
13. Henzler-Wildman, K. A., Thai, V., Lei, M., Ott, M., Wolf-Watz, M., Fenn, T., Pozharski, E., Wilson, M. A., Petsko, G. A., and Karplus, M. (2007) Intrinsic motions along an enzymatic reaction trajectory, Nature 450, 838-844.
14. Santoso, Y., Joyce, C. M., Potapova, O., Le Reste, L., Hohlbein, J., Torella, J. P., Grindley, N. D., and Kapanidis, A. N. (2010) Conformational transitions in DNA polymerase I revealed by single-molecule FRET, Proc. Natl. Acad. of Sci. U.S.A. 107, 715-720.
15. Boehr, D. D., McElheny, D., Dyson, H. J., and Wright, P. E. (2006) The dynamic energy landscape of dihydrofolate reductase catalysis, Science 313, 1638-1642.
16. Henrissat, B. (1991) A classification of glycosyl hydrolases based on amino-acid-sequence similarities, Biochem. J. 280, 309-316.
17. Saha, B. C. (2003) Hemicellulose bioconversion, J. Ind. Microbiol. Biotechnol. 30, 279-291.
18. Polizeli, M., Rizzatti, A., Monti, R., Terenzi, H., Jorge, J. A., and Amorim, D. (2005) Xylanases from fungi: properties and industrial applications, Appl. Microbiol. Biotechnol. 67, 577-591.
19. Paës, G., Berrin, J.-G., and Beaugrand, J. (2012) GH11 xylanases: structure/function/properties relationships and applications, Biotechnol. Adv. 30, 564-592.
20. Paës, G., Tran, V., Takahashi, M., Boukari, I., and O'donohue, M. J. (2007) New insights into the role of the thumb-like loop in GH-11 xylanases, Protein Eng. Des. Sel. 20, 15-23.
21. Wakarchuk, W. W., Campbell, R. L., Sung, W. L., Davoodi, J., and Yaguchi, M. (1994) Mutational and crystallographic analyses of the active site residues of the Bacillus circulans xylanase, Protein Sci. 3, 467-475.
22. Plesniak, L. A., Mcintosh, L. P., and Wakarchuk, W. W. (1996) Secondary structure and NMR assignments of Bacillus circulans xylanase, Protein Sci. 5, 1118-1135.
23. Davies, G. J., Wilson, K. S., and Henrissat, B. (1997) Nomenclature for sugar-binding subsites in glycosyl hydrolases, Biochem. J. 321, 557.
24. Rye, C. S., and Withers, S. G. (2000) Glycosidase mechanisms, Curr. Opin. Chem. Biol. 4, 573-580.
25. Mhlongo, N. N., Ebrahim, M., Skelton, A. A., Kruger, H. G., Williams, I. H., and Soliman, M. E. S. (2015) Dynamics of the thumb-finger regions in a GH11 xylanase Bacillus circulans: comparison between the Michaelis and covalent intermediate, RSC Advances 5, 82381-82394.

26. Paës, G., Cortés, J., Siméon, T., O'Donohue, M. J., and Tran, V. (2012) Thumb-loops up for catalysis: a structure/function investigation of a functional loop movement in a GH11 xylanase, Comput. Struct. Biotechnol. J. 1, e201207001.
27. Murakami, M. T., Arni, R. K., Vieira, D. S., Degrève, L., Ruller, R., and Ward, R. J. (2005) Correlation of temperature induced conformation change with optimum catalytic activity in the recombinant G/11 xylanase A from Bacillus subtilis strain 168 (1A1), FEBS Lett. 579, 6505-6510.
28. Paës, G., Cortés, J., Siméon, T., O'Donohue, M. J., and Tran, V. (2012) Thumb-loops up for catalysis: a structure/function investigation of a functional loop movement in a GH11 xylanase, Comput. Struct. Biotechnol. J. 1, 1-10.
29. Pollet, A., Vandermarliere, E., Lammertyn, J., Strelkov, S. V., Delcour, J. A., and Courtin, C. M. (2009) Crystallographic and activity-based evidence for thumb flexibility and its relevance in glycoside hydrolase family 11 xylanases, Proteins 77, 395-403.
30. Gagné, D., Narayanan, C., Nguyen-Thi, N., Roux, L. D., Bernard, D. N., Brunzelle, J. S., Couture, J.-F., Agarwal, P. K., and Doucet, N. (2016) Ligand binding enhances millisecond conformational exchange in xylanase B2 from Streptomyces lividans, Biochemistry 55, 4184-4196.
31. Muilu, J., Törrönen, A., Peräkylä, M., and Rouvinen, J. (1998) Functional conformational changes of endo-1, 4-xylanase II from Trichoderma reesei: A molecular dynamics study, Proteins 31, 434-444.
32. Sidhu, G., Withers, S. G., Nguyen, N. T., McIntosh, L. P., Ziser, L., and Brayer, G. D. (1999) Sugar ring distortion in the glycosyl-enzyme intermediate of a family G/11 xylanase, Biochemistry 38, 5346-5354.
33. Connelly, G. P., Withers, S. G., and McIntosh, L. P. (2000) Analysis of the dynamic properties of Bacillus circulans xylanase upon formation of a covalent glycosyl-enzyme intermediate, Protein Sci. 9, 512-524.
34. Ludwiczek, M. L., Heller, M., Kantner, T., and McIntosh, L. P. (2007) A secondary xylan-binding site enhances the catalytic activity of a single-domain family 11 glycoside hydrolase, J. Mol. Biol. 373, 337-354.
35. Waudby, C. A., Ramos, A., Cabrita, L. D., and Christodoulou, J. (2016) Two-dimensional NMR lineshape analysis, Sci. Rep. 6, 24826.
36. Zechel, D. L., Konermann, L., Withers, S. G., and Douglas, D. (1998) Pre-steady state kinetic analysis of an enzymatic reaction monitored by time-resolved electrospray ionization mass spectrometry, Biochemistry 37, 7664-7669.
37. Wan, Q., Zhang, Q., Hamilton-Brehm, S., Weiss, K., Mustyakimov, M., Coates, L., Langan, P., Graham, D., and Kovalevsky, A. (2014) X-ray crystallographic studies of family 11 xylanase Michaelis and product complexes: implications for the catalytic mechanism, Acta Crystallogr. Sect. D. Biol. Crystallogr. 70, 11-23.
38. Havukainen, R., Törrönen, A., Laitinen, T., and Rouvinen, J. (1996) Covalent binding of three epoxyalkyl xylosides to the active site of endo-1, 4-xylanase II from Trichoderma reesei, Biochemistry 35, 9617-9624.
39. Igarashi, K., Koivula, A., Wada, M., Kimura, S., Penttilä, M., and Samejima, M. (2009) High speed atomic force microscopy visualizes processive movement of Trichoderma reesei cellobiohydrolase I on crystalline cellulose, J. Biol. Chem. 284, 36186-36190.
40. Schröder, S. P., Petracca, R., Minnee, H., Artola, M., Aerts, J. M., Codée, J. D., Van Der Marel, G. A., and Overkleeft, H. S. (2016) A Divergent Synthesis of l-arabino-and d-xylo-Configured Cyclophellitol Epoxides and Aziridines, Eur. J. Org. Chem. 2016, 4787-4794.
41. Lee, W., Tonelli, M., and Markley, J. L. (2014) NMRFAM-SPARKY: enhanced software for biomolecular NMR spectroscopy, Bioinformatics 31, 1325-1327.
42. Schmitz, C., Stanton-Cook, M. J., Su, X.-C., Otting, G., and Huber, T. (2008) Numbat: an interactive software tool for fitting Δχ-tensors to molecular coordinates using pseudocontact shifts, J. Biomol. NMR 41, 179.
43. Bashir, Q., Volkov, A. N., Ullmann, G. M., and Ubbink, M. (2009) Visualization of the encounter ensemble of the transient electron transfer complex of cytochrome c and cytochrome c peroxidase, J. Am. Chem. Soc. 132, 241-247.
44. Loria, J. P., Rance, M., and Palmer, A. G. (1999) A relaxation-compensated Carr−Purcell− Meiboom−Gill sequence for characterizing chemical exchange by NMR spectroscopy, J. Am. Chem. Soc. 121, 2331-2332.
45. Hansen, D. F., Yang, D., Feng, H., Zhou, Z., Wiesner, S., Bai, Y., and Kay, L. E. (2007) An exchange-free measure of 15N transverse relaxation: an NMR spectroscopy application to the study of a folding intermediate with pervasive chemical exchange, J. Am. Chem. Soc. 129, 11468-11479.